Early presence of Homo sapiens by 86-68 kyrs in Southeast Asia at Tam Pà Ling cave, Northern Laos.

Sarah Freidline, Kira Westaway, Renaud Joannes-Boyau, Philippe Duringer, Jean-Luc Ponche, Mike Morley, Vito Paolo Hernandez, Meghan Mcallister-Hayward, Hugh Mccoll, Clément Zanolli, et al.

To cite this version:

Sarah Freidline, Kira Westaway, Renaud Joannes-Boyau, Philippe Duringer, Jean-Luc Ponche, et al.. Early presence of Homo sapiens by 86-68 kyrs in Southeast Asia at Tam Pà Ling cave, Northern Laos.. 2023. hal-04043069

HAL Id: hal-04043069
https://hal.science/hal-04043069v1

Preprint submitted on 23 Mar 2023

Early presence of Homo sapiens by 86-68 kyrs in Southeast Asia at Tam Pà Ling cave, Northern Laos.

Sarah Freidline
University of Central Florida https://orcid.org/0000-0003-4872-4924
Kira Westaway
Macquarie University https://orcid.org/0000-0001-5315-778X
Renaud Joannes-Boyau
Southern Cross University https://orcid.org/0000-0002-0452-486X
Philippe Duringer
Ecole et Observatoire des Sciences de la Terre (EOST), Institut de Physique du Globe de Strasbourg (IPGS), UMR 7516 CNRS, Université de Strasbourg
Jean-Luc Ponche
LMSPC,
Mike Morley
Flinders University
Vito Paolo Hernandez
Flinders University https://orcid.org/0000-0003-0295-6068
Meghan McAllister-Hayward
Flinders University
Hugh McColl
University of Copenhagen https://orcid.org/0000-0002-7568-4270
Clément Zanolli
Université de Bordeaux https://orcid.org/0000-0002-5617-1613
Philipp Gunz
Max Planck Institute for Evolutionary Anthropology https://orcid.org/0000-0002-2350-4450
Inga Bergmann
Max Planck Institute for Evolutionary Anthropology
Phonephanh Sichanthongtip
Department of National Heritage Ministry of Information and Culture
Daovee Sihanam
Department of Heritage, Ministry of Information, Culture and Tourism
Souliphane Boualaphane
Department of Heritage, Ministry of Information, Culture and Tourism
Thonglith Luangkhoth
Department of Heritage, Ministry of Information, Culture and Tourism
Viengkeo Souksavatdy
Department of Heritage, Ministry of Information, Culture and Tourism
Anthony Dosseto
University of Wollongong https://orcid.org/0000-0002-3575-0106
Quentin Boesch
Ecole et Observatoire des Sciences de la Terre (EOST) Institut de Physique du Globe de Strasbourg (IPGS) UMR 7516 CNRS Université de Strasbourg
Elise Patole-Edoumba
Museum d'Histoire naturelle
Françoise Aubaile

Musee de l'Homme

Françoise Crozier
IRD, DIADE

Eric Suzzoni
Spitteurs Pan, technical cave supervision and exploration

Sébastien Frangeul
Spitteurs Pan, technical cave supervision and exploration

Nicolas Bourgon
Max Planck Institute for Evolutionary Anthropology https://orcid.org/0000-0001-8538-1903

Alexandra Zachwieja
Department of Biomedical Sciences, Medical School, University of Minnesota

Tyler Dunn
Oregon Health Science University

Anne-Marie Bacon
Paris Descartes University

Jean-Jacques Hublin
College de France

Laura Shackelford
University of Illinois at Urbana-Champaign https://orcid.org/0000-0002-0934-2360

Fabrice Demeter (✉ **f.demeter@sund.ku.dk**)
University of Copenhagen

Article

Keywords: Southeast Asia, Homo sapiens, geometric morphometrics, Late Pleistocene, brow ridge, mandible

Posted Date: January 16th, 2023

DOI: https://doi.org/10.21203/rs.3.rs-2410300/v1

Abstract

The timing of the first arrival of *Homo sapiens* in East Asia from Africa and the degree to which they interbred with or replaced local archaic populations is controversial. Previous discoveries from Tam Pà Ling cave (Laos) identified *H. sapiens* in Southeast Asia by 46 kyr. We report on a new frontal bone (TPL 6) and slightly older tibial fragment (TPL 7) discovered in the deepest layers of TPL. Bayesian modeling of luminescence dating of sediments and U-series and combined U-series-ESR dating of mammalian teeth reveals a depositional sequence spanning ~ 86 kyr. TPL 6 confirms the presence of *H. sapiens* by 70 ± 3 kyr, and TPL 7 extends this range to 77 ± 9 kyr, supporting an early dispersal of *H. sapiens* into Southeast Asia. Geometric morphometric analyses of TPL 6 suggest descent from a gracile immigrant population rather than evolution from or admixture with local archaic populations.

Introduction

Current genetic and fossil evidence points to an African origin of *Homo sapiens* around 300 kyr [1,2]. The number, timing, and route(s) of human dispersal out of Africa into Eurasia is intensely debated (see refs[3–6] for review) with dispersal models falling into two broad categories: an early dispersal during Marine Isotope Stage (MIS) 5 (~ 130–80 kyr) and a late dispersal occurring in a post-MIS 5 time frame[3]. Genomic evidence strongly supports a single rapid dispersal of all ancestral non-African *H. sapiens* populations after 50 to 60 kyr followed by a divergence of descendant groups westward into Europe and eastward into South Asia[1,7,8]. While there is some genetic evidence supporting a separate, early worldwide expansion of *H. sapiens* in present day Australasian populations (i.e., Australians, New Guineans and Asian "Negrito"),[9–12] recent genomic studies on ancient and extant humans suggest that if there was any genetic contribution of such early dispersals to present-day populations it was not substantial, being less than 1%[13–18].

Fossil and archaeological evidence for early range expansions include the famous sites of Skhul and Qafzeh in Israel and more recent finds in the eastern Mediterranean, Arabian Peninsula, East and Southeast Asia, and Australia. Fossils from Apidima Cave in Greece[19] and Misliya Cave in Israel[20], dated to around 210 kyr and 180 kyr respectively, have been described as the earliest *H. sapiens* outside of Africa predating the Skhul and Qafzeh fossils by at least 60,000 years, and in Saudi Arabia a phalanx from Al Wusta is dated to ca. 90 kyr[21]. Further East, fossils predating 50 kyr are mainly teeth from the Chinese sites of Fuyan Cave (120 – 80 kyr)[22,23], Huanglongdong (100 – 80 kyr)[24,25], Lunadong (127 – 70 kyr)[26], and Zhirendong (116 – 106 kyr)[27–29]. A recent attempt to verify the dating of several of these sites by Sun et al.[30] presented a number of issues including inaccurate radiocarbon estimations, misattribution to *Homo* of a sampled tooth, potential contamination in genetic analyses and incorrect provenience[31,32]. Similarly, the modern looking cranium from Liujiang has been dated within the range of ca. 139 to 68 kyr[33,34], however its provenience is uncertain. Other Late Pleistocene sites where modern humans were found include Lida Ajer in Sumatra, dated to 73 – 63 kyr[35], which yielded two teeth attributed to *H. sapiens*, and Tam Pà Ling in northern Laos, where a handful of cranio-mandibular and more fragmentary postcranial remains span the period of 70 – 46 kyr[36,37]. Finally, Madjedbebe, the oldest archaeological site in Australia is dated to 65 kyr[38]. Taken together these findings suggest a more complex pattern of dispersal that is hard to reconcile with current genetic evidence unless these early dispersals represent unsuccessful colonizations.

Here, we report on new fossil and chronological evidence from Tam Pà Ling (TPL; Supplementary Information, Location; Supplementary Fig. 1) that confirms an early dispersal of *H. sapiens* into mainland Southeast Asia during late MIS 5. The new, undescribed partial frontal bone (TPL 6, Fig. 1), along with a tibial fragment (TPL 7; Fig. 2), are currently the oldest fossils from this site, older than 70 kyr. The site, Tam Pà Ling, was discovered in 2009 when a partial cranium (TPL 1) was unearthed and since then, in addition to TPL 6 and 7, two mandibles (TPL 2 and 3), a rib (TPL 4), and a phalanx (TPL 5) have been recovered. Quantitative analyses on the mandibles and associated dentition suggest that the previously found fossils from TPL are clearly *H. sapiens* with some retained archaic features[36,37,39,40].

A chronological framework has been established for TPL 1–5 using a combination of radiocarbon, U-series, US-ESR and luminescence dating and spans the age range of 70 – 46 kyr. This first framework has been detailed elsewhere[36,37,39,40] but is briefly summarized here (Stratigraphic section Fig. 3). The absence of precipitated flowstone and the issues of non-*in situ* charcoal combined with a sparsity of faunal teeth in the sedimentary section meant that luminescence dating applied to the sediments has become the backbone of the chronology. Optically stimulated luminescence (OSL) and red thermoluminescence (red TL) were initially applied to sediments in the upper levels (0-2.5 m TPLOSL4-8) that aligned with the original fossils (TPLOSL1-2) of the skull (TPL1) and mandible (TPL2) at 2.5-3.0 m providing an age range of 46 ± 2 kyr. These results display stratigraphic integrity from 1–3 m and a steady increase in age with depth over a ~ 30 kyr period from 1.5–2.5 m and agree with a maximum U/Th age of 64 ± 1 kyr for the tip of a stalactite that was precipitated prior to being buried in sediments[39].

Two additional OSL samples collected between 4.0–5.0 m (TPLOSL 3, 10) produced a similar age (48 ± 5 kyr) despite a large increase in depth. This suggested that the age of the deepest layers may be slightly underestimated due to the saturation limits of quartz OSL dating that occurs at 3–4 m (~ 46 kyr or equivalent to 300 Gy). This issue was addressed in Shackelford et al.[37] by applying post infrared infrared-stimulated luminescence (pIR- IRSL) dating to feldspars to provide an independent age control for the quartz chronology. This feldspar chronology is coeval with the established quartz chronology until ∼3 m (sample TPLOSL-2) but then increases in antiquity to ∼4 m (TPLOSL-3) and ~ 5 m (TPLOSL10) and beyond. Other supporting evidence for the antiquity of the fossils includes a single U-series dating of the TPL1 frontal bone and a bone fragment from the TPL2 mandibular condyle. Neither of these samples provided the opportunity for U-series profiling to establish the integrity of the result and thus provided only minimum ages of 63 kyr[36] and 44–36 kyr[39], respectively.

In this paper, we extend the TPL chronology beyond 5 meters with new luminescence dating on the deepest sediments, apply Uranium series and US-ESR combined dating to mammalian teeth (see Supplementary Fig. 7), present a new modeled chronological framework for the site, and report on a new frontal bone, TPL 6, from this area of the cave. We use semilandmark geometric morphometric methods to compare the shape and size of the TPL craniomandibular remains (TPL 1, 2, 3, and 6) to a large sample of Early to Late Pleistocene fossils from Africa and Eurasia as well as Southeast Asian Holocene humans. The remains from Tam Pà Ling provide insight to temporal trends in facial and mandibular morphology in a sparse Late Pleistocene Southeast Asian fossil record. Furthermore, as Tam Pà Ling is situated in a potential migratory path into Australasia and Northern Asia, the morphology of the TPL fossils can improve our knowledge of the timing and route of dispersal of *H. sapiens* into East Asia and eventually Australia, as well as the nature of interaction of *H. sapiens* with local archaic populations (i.e., admixture).

Results

Context and Dating

The geological setting and stratigraphy of Tam Pà Ling, discussed together with the magnetic susceptibility and total carbon content of its sediment, outlines the gradual opening of the cave from at least 77 ± 9 kyr and predominantly low-energy and monsoon-driven site formation processes in the investigated areas of the cave (Supplementary Information, Geology; Supplementary Figs. 3–6 and Supplementary Tables 1 and 2). Slabs from cave roof-fall associated with small clasts of limestone and comminuted rock powder in the sedimentary sequence provide the primary evidence for the gradual opening of Tam Pà Ling, which generally coincides with drier climatic conditions from MIS 5–2. The East Asian Monsoon (EAM) from at least MIS 5 has influenced much of the sedimentation in the cave with colluviation as the primary mode of fine sediment delivery.

The Uranium concentration in the fossil teeth enamel for direct dating was weak, but consistent and homogenous in the dentine for both samples. These provide average minimum ages of 64.1 ± 1.3 kyr and 67.3 ± 1.3 kyr for TPL-01 and TPL-02, respectively, found at 6.40 m and 6.67 m (Table 1). Using the raster sequence, we have modeled each tooth with Diffusion-Adsorption-Decay (DAD; Fig. 4A and Table 2), which takes into consideration the diffusion rate and size of each dental tissue[41,42].

Following the U-series dating, TPL-02 underwent ESR measurements. The dose reconstruction curve obtained on the merge signal on the enamel fragment gave a D_e of 160.1 +/-7.3 Gy after subtraction of a 17% NOCOR ratio according to the protocol of Joannes-Boyau[43]. A US-ESR age of 84 +/-8 kyr was then obtained using the parameters detailed in Fig. 4B.

We used two different protocols for the estimation of the luminescence dose rate: a combination of alpha and beta counting (Table 3A) plus a high-resolution gamma spectrometry technique (Table 3B). The latter technique produced dose rates that were on average 0.1–0.3 Gy/kyr lower than the alpha and beta counting approach. Age estimates were calculated using both approaches to illustrate the slight difference in ages, which are negligible within error limits.

According to the new pIR-IRSL age estimates from TPLOSL12-15, the fossils found between 5.72–6.67 m (TPL3,4,6) range from 67 ± 5 kyr to 80 ± 10 kyr. This age range is supported by the poly-mineral fine grain chronology from 65 ± 20 kyr to 86 ± 12 kyr, and by the direct dating of mammalian teeth ranging from 67 ± 2 kyr – 84 ± 8 kyr.

Considering the TPL chronology as a whole, there are now a total of 33 radiometric ages extending over ~ 7 m of sediment. The applied Bayesian modeling reveals a depositional sequence that spans ~ 86 kyr within errors from 2 ± 0.8 to 77 ± 9 ka (at 2 σ), with the presence of human material extending for ~ 56 kyr within errors from 39 ± 9–77 ± 9 ka (Fig. 5). The oldest discovered fossil (TPL7) at 6.97 m may be older than the modeled age of 77 ± 9 ka as the deepest sediment sample (TPL15) was collected 30 cm higher at 6.67 m.

Geometric Morphometric Shape Analysis Of The Craniomandibular Remains

Tam Pà Ling 1 & 6 Frontals

The TPL 6 reconstructions and TPL 1 were projected into the first two dimensions of the principal component analysis (PCA) in shape space, which explains 71% of shape variance (Fig. 6A left panel). Most groups separate along principal component (PC) 1, which documents shape changes associated with the brow ridge and frontal squama and is correlated with allometric size (r = 0.73). Main shape changes along PC 1 are the projection and shape of the brow ridge, and rounding of the frontal squama, with specimens plotting at the positive end of PC 1 (i.e., *H. erectus*) expressing an entirely more robust and projecting brow ridge, narrower frontal width, and a flatter and more receding frontal squama. In contrast, specimens plotting along the negative end of PC 1, including the TPL 6 reconstructions, have a brow ridge morphology that is much more gracile and a vertical frontal bone. The TPL 6 reconstructions cluster together and near to several Holocene individuals and fossils from the site of Minatogawa, Japan (A, 1, and 4). TPL 1 falls clearly within *H. sapiens* variation, plotting near to the Australasian Late Pleistocene fossils from Wadjak, Lake Mungo, Salkhit, and Zhoukoudian UC 101. Evaluation of higher PCs shows greater overlap between groups. PCA (Fig. 6A right panel) and between-group PCA (bgPCA; Supplementary Fig. 8) on only the *H. sapiens* sample (early, Late, and Holocene) supports these results, and cross-validated linear discriminate analysis classifies (Supplementary Table 3) all TPL 6 reconstructions as Holocene *H. sapiens* (posterior probability ranging from 66–82%) and TPL 1 as Late Pleistocene (posterior probability 64.7%). According to Procrustes distances (Supplementary Table 4) and centroid sizes (Supplementary Fig. 9), TPL 6's frontal shape and size is most similar to the Late Pleistocene specimens Minatogawa A and 4 and Southeast Asian Holocene *H. sapiens*. It is small and its brow ridge is gracile with a projecting lateral component and a wide but flattened frontal squama (Supplementary Fig. 10). The latter features it shares with TPL 1. TPL 1 is larger and more robust than TPL 6 with a more projecting glabella and medial brow ridge. Its overall shape and proportions are most similar to Australasian Late Pleistocene *H. sapiens* Zhoukoudian UC 101, Tabon, and Lake Mungo.

Tam Pà Ling 1 Maxilla

All groups overlap along PC 1 in the PCA in shape space on the maxillary data set (Fig. 6B left panel). PC 2, which is more strongly correlated with centroid size (r = 0.30 and r = 0.69, respectively), separates Neanderthals from Late Pleistocene and Holocene *H. sapiens* with the early *H. sapiens* plotting in between the two extremes. The TPL 1 maxilla plots within the range of Late Pleistocene and Holocene *H. sapiens* variation and near to Liujiang 1, Zhoukoudian UC 101, and Laetoli Hominin 18. The maxillary morphology of the Neanderthals plotting along the negative end of PC 2 is characterized by a more vertical subnasal region, posteriorly positioned zygomatic root, and a narrower palate. In contrast, *H. sapiens* such as Minatogawa 4 have subnasal morphology that is more posteriorly sloped, an anteriorly positioned zygomatic root, and a broader palate. Although not as extreme as Minatogawa 4, TPL 1 follows the *H. sapiens* pattern of a sloping subnasal region and a broader palate. Its nearest neighbors include early (Qafzeh 6), Late Pleistocene (Liujiang), and Holocene *H. sapiens* (Supplementary Table 5). In the PCA and bgPCA on only the *H. sapiens* sample (Fig. 6B right panel, Supplementary Fig. 11, respectively), TPL 1 plots alongside early *H. sapiens*, and in cross-validated linear discriminant analysis it is classified (Supplementary Table 3) as an early *H. sapiens* (posterior probability 88.0%). TPL 1 has a prognathic anterior maxilla similar to early *H. sapiens* (Supplementary Fig. 12), and a broad and deep palate like all *H. sapiens* (early, Late Pleistocene, and Holocene). Like frontal bone size, there is a clear difference in centroid size in archaic hominins, including early *H. sapiens* and later *H. sapiens* (i.e., Late Pleistocene and Holocene; Supplementary Fig. 13). The centroid size of TPL 1 is large, falling near the top of the Late Pleistocene upper quartile, but much smaller than early *H. sapiens* and archaic humans.

Tam Pà Ling 2 Mandible

The original and new reconstruction of the TPL 2 mandible were projected into a PCA in shape space (Fig. 7A left panel). There is a clear separation between Late Pleistocene and Holocene *H. sapiens* and Neanderthals and *H. erectus* along the first two PCs, and the early *H. sapiens* plot intermediate between these two extremes and overlap with all groups. Both TPL reconstructions plot within early *H. sapiens* variation; the new reconstruction is closer to the Late Pleistocene and Holocene *H. sapiens* range of variation, plotting nearest to Tianyuandong and Tam Pong among the fossils. Specimens plotting towards the negative end of PC 1, which include some Neanderthals, early *H. sapiens*, and *H. erectus*, have a narrow mandibular breadth, tall anterior symphysis, thinner lateral corpus, and larger ramus and coronoid process. The Holocene *H. sapiens* show the opposite condition, and the TPL 2 mandibles plot in the middle expressing an intermediate shape. PCA and bgPCA on only the *H. sapiens* sample (Fig. 7A right panel, Supplementary Fig. 14, respectively) support these results, and linear discriminant analysis classifies (Supplementary Table 3) both TPL 2 reconstructions as Holocene *H. sapiens* (posterior probability ranging from 51.8–91.4%). According to inter-individual Procrustes distances (Supplementary. Table 6), both TPL 2 reconstructions are most similar to Holocene humans from Tam Hang South and the Late Pleistocene specimen Tam Pong 1. While its ramal shape is most similar to Late Pleistocene *H. sapiens* (Supplementary Fig. 15), it has an extremely robust corpus and one of the smallest centroid sizes in the sample (Supplementary Fig. 16).

Tam Pà Ling 2 And 3 Anterior Corpus

The PCA in shape space on the anterior corpus dataset shows a clearer separation between *H. erectus* and Liang Bua 1 and all other groups (Fig. 7B left panel). Neanderthals are intermediate between *H. erectus* and *H. sapiens* along PC 1, but there is significant overlap between these groups. Specimens plotting along the negative end of PC 1 (early, Late, and Holocene *H. sapiens*) have a pronounced chin and a shorter symphysis height, whereas *H. erectus* and Liang Bua have a taller, receding symphysis that lacks a chin. Both TPL 2 reconstructions and TPL 3 are similar in this morphology, expressing the *H. sapiens* pattern. The TPL 2 reconstructions have a taller and thinner corpus compared to TPL 3, which has a pronounced chin and shorter corpus height. In anterior corpus shape, the TPL 2 reconstructions are most similar to early (Tabun 2; Dar es-Soltane 5), Late Pleistocene (Wadjak 2 and Zhoukoudian Upper Cave 101), and Holocene *H. sapiens* (Supplementary Fig. 17), while TPL 3 is nearest neighbors with Late Pleistocene (Zhoukoudian Upper Cave 101 and Minatogawa 1) and Holocene *H. sapiens*, as well as Neanderthals (Guattari 3 and La Ferrassie 1; Supplementary Table 7). PCA and bgPCA on only the *H. sapiens* sample (Fig. 7B right panel, Supplementary Fig. 18, respectively) support these results, and cross-validated linear discriminant analysis classifies (Supplementary Table 3) both TPL 2 reconstructions as Holocene *H. sapiens* (posterior probability ranging from 44.2% to 59.4) and TPL 3 as early *H. sapiens* (posterior probability 35.5%). The TPL 3 anterior corpus is within the size range of Late Pleistocene and Holocene *H. sapiens* (Supplementary Fig. 19), whereas TPL 2 falls outside of the interquartile range for all groups yet is comparable in size to several early *H. sapiens* fossils (Klasies River 41805 and Border Cave 2) and Late Pleistocene Asian fossils (Zhirendong 3 and Minatogawa A).

Postcranial Element From Tam Pà Ling

TPL 7 Tibia

TPL7 was found in 2018. It is a human proximal diaphyseal fragment of a left tibia with considerable taphonomic alteration (Fig. 2). The fragment is 98 mm at its maximum length and roughly triangular in cross-section. The proximal end of the fragment maintains the most distal end of the tibial tuberosity anteriorly as evidenced by the slight rugosity at the most superior aspect of the anterior crest and the broadening of the anterior aspect of the proximal cross-section. Posteriorly, it retains the most proximal part of the vertical line. Laterally, there is a distinct interosseous crest that sharpens distally.

All the bone surfaces are uniformly bleached with several fractures throughout. There are four large longitudinal fractures running the length of the fragment and extending from the periosteal to the endosteal surface. The periosteal surface has several micro- and macro-fractures resulting in a broadly rough and fibrous texture. There are several areas of cortical exfoliation throughout. All fracture margins have a rough, jagged appearance, an indication that they are the result of taphonomic processes. The fracture margins and medullary cavity are impacted with a reddish-brown matrix.

Taphonomic alteration of the element precludes accurate osteometric analysis. However, though fragmented with the anterior portion slightly medially offset, the shaft is bound by matrix into a near intact position allowing for approximate dimensions. Proximally, the tibia has a maximum anteroposterior (AP) diameter of 32.6 mm and maximum mediolateral (ML) diameter of 22.9 mm. It tapers distally where it has a more circular profile (AP diameter = 28.6 mm; ML diameter = 26.1 mm). TPL7 maintains a relatively thick cortical bone and a slim medullary cavity (Fig. 2), which is visible due to the broken ends of the bone. At its thickest, the cortical bone is 17.04 mm on the proximal anterior surface of the fragment.

Discussion

An extended chronology for Tam Pà Ling

The results of the new sediment and tooth samples combined with the first modeling of the site incorporating the age estimates for five independent dating techniques has extended the chronology by ~ 10 kyr and revealed that humans were present in this area for ~ 56 kyr. The modeling vindicates the stratigraphic integrity of the site and its associated fossils.

Regarding the direct dating, the mean U-series age and DAD age are not within errors, yet in close range, advocating for an early uptake of uranium into the dental tissues. It appears likely that both teeth, while in close age range, are from two separate depositional episodes, with TPL-02 older than TPL-01. This is reinforced by the $^{234}U/^{238}U$ ratio which diverges between the two samples, indicating either two distinct uranium diffusion episodes or two separate sources. The US-ESR age, while slightly older, remains in agreement with the DAD modeled age of TPL-02. With only two U-series samples and one US-ESR sample the corpus remains limited to properly assess the age of the site, yet all dating results show consistency with a conservative likely age range for Tam Pà Ling fossils between 92 – 65 kyr (by combining both US-ESR and U-series dating results).

The luminescence dating became increasingly complex with depth down the section. By ~ 4 m the quartz had completely saturated as demonstrated by the divergence between the OSL-SG and pIR-IRSL ages from samples TPL3 and 10. This necessitated the use of a feldspar chronology; however, by ~ 6 m it became clear that the feldspar grains were becoming increasingly weathered (as identified using a light microscope after measurement) with a dramatic reduction in the number of usable grains. This necessitated the use of poly-mineral fine-grained dating[44,45] as a supportive data set. This technique slightly underestimates the coarse-grained feldspar results with slightly larger errors (for samples TPL13-14) but was coeval within error margins.

Not only have we extended the chronology for the site with the new TPL12-15 age estimates, but we have for the first time included direct dating of mammalian teeth. This was not possible previously due to the lack of available fossils for dating. Now that we see good agreement between the sediment and fossil chronologies, we feel more confident modeling the chronology using the Bayesian techniques described. This provides a more definitive chronology and integrity for the site and its associated fossil evidence. The modeled chronology confirms that far from representing a rapid deposition, the site represents a slow and seasonal accumulation of sediment over ~ 86 kyrs, with the human evidence accumulating over a 56 kyr period.

Morphology Of The Tam Pà Ling Hominins And Its Implications

Our shape analysis of the TPL 6 frontal places *H. sapiens* in continental Southeast Asia by at least 67 kyr. The TPL fossils' clear affinities to *H. sapiens* suggest that they descended from a gracile *H. sapiens* population from Africa and/or the Near East. The earliest evidence of *H. sapiens* in Asia is found at Misliya Cave, Israel, and dated to 194 – 177 kyr[20]. The main phase of *H. sapiens* expansion into Asia, however, occurs around 50 kyr as the genomic evidence points to a single rapid dispersal of all ancestral non-African populations around 65 to 45 kyr[1,7,8]. This is true of the oldest of all ancient and modern human genomes from across Eurasia including the oldest 11 ancient human genomes dated between 45 – 35 kyr[46–51]. Within Southeast Asia, ancient DNA has shown that although the earlier hunter gatherer populations were largely replaced by incoming farmers around 4 kyr, the genetic diversity of both populations fall within that of the single rapid dispersion out of Africa[52,53]. The age range of TPL 1, 2 and 3 fall within this period. TPL 6, with an age of 73 – 67 kyr, joins the other hotly debated fossils from southern and central China (e.g., Huanglong, Zhiren, Luna and Fuyan) that suggest an earlier, possibly failed, dispersal. Therefore, the post MIS 5 fossils from Tam Pà Ling can either be interpreted as descendants of the TPL 6 lineage that did not contribute to the present-day human gene pool or as early descendants of the larger, successful dispersal of *H. sapiens* into Southeast Asia. Unfortunately, these fossils do not preserve ancient DNA to directly test these hypotheses.

Our shape analyses are consistent with previous studies attributing the Tam Pà Ling fossils to *H. sapiens*[36,37,39]. Among the Late Pleistocene *H. sapiens* sample, the TPL fossils are most similar to Zhoukoudian Upper Cave 101, Minatogawa (1 and A), Liujiang, and Tabon. Our results support previous observations that high levels of heterogeneity characterize Late Pleistocene modern human groups[54,55]. Considerable shape and size variability is present at Tam Pà Ling, as well as at Zhoukoudian Upper Cave and Minatogawa. The TPL 6 frontal and TPL 2 mandible are small compared to all groups except for *H. floresiensis* (Liang Bua 1), while the TPL 1 face (frontal and maxilla) and TPL 3 anterior corpus is clearly within the range of Late Pleistocene *H. sapiens*. Interestingly, the younger TPL 1 frontal is larger and more robust than the remarkably gracile TPL 6 frontal. If the TPL hominins are all descendants of an early dispersal of *H. sapiens* from Africa, then the robust features in TPL 1, as well as the mandibles, TPL 2 and 3, may have been independently acquired due to local evolution through isolation and genetic drift. Their clear shape affinities to *H. sapiens* and distinction from archaic hominins (e.g., Neanderthals and *H. erectus*) challenges hybridization with endemic species (e.g., Denisovan, *H. floresiensis*, *H. luzonensis*, and *H. erectus*) as the likely explanation for their robust morphology.

TPL 6 is the oldest cranial fossil recovered from Tam Pà Ling. It is smaller and more gracile than TPL 1, and its shape is most similar to Minatogawa A, a Late Pleistocene *H. sapiens* from Japan (dated to ca. 18 kyr or as recent ca. 8 kyr[56,57]), as well as Holocene *H. sapiens* from Vietnam. Among the Minatogawa remains, the more complete skeleton Minatogawa 1 is considered a robust male and the smaller, Minatogawa A mandible is considered a female[57]. The Minatogawa fossils have been described as showing closer morphological affinities to southern Asians (e.g., Australo-Melanesians, and fossils from Liujiang, Niah Cave, and Wadjak) than northern Asians[57–59]. Both the size and shape differences between TPL 1 and 6 are comparable to the differences found between Minatogawa 1 and A. However, unlike Minatogawa there is a temporal separation between TPL 1 and 6 of around 30,000 years. Therefore, while their shape and size differences could reflect sexual dimorphism, diachronic changes and interbreeding with more robust *H. sapiens* cannot be ruled out. However, TP6's shape affinities to Minatogawa A, Holocene humans, and the younger TPL fossils, like TPL 1 must be interpreted within the context of the current genetic evidence which does not support regional continuity of *H. sapiens* in Asia from MIS 5 on. Under this scenario, TPL 6 and potentially the younger fossils from Tam Pà Ling would represent an unsuccessful dispersal. Whether this dispersal disappeared prior to the main later dispersal, or the distinct migrations experienced a period of co-habitation remains unclear with absence of ancient DNA from 50 kyr to 10 kyr. By 7.8 kyr at Pha Faen, Laos, the earliest genome from Southeast Asia shows no genetic evidence of an early dispersal[53]. Shape similarities to later humans (e.g., Minatogawa) are likely attributed to their small frontal bone size (Supplementary Fig. 9; PC 1 is correlated with centroid size $r = 0.73$ and frontal size explains approximately 32% of shape variance and is highly significant [adjusted R-squared = 0.33, degrees of freedom = 75, $F = 37.11$, $p < 0.001$]).

Following TPL 6, the next oldest cranio-mandibular fossil from Tam Pà Ling is TPL 3, an anterior corpus dated to ca. 70 kyr. In a previous geometric morphometric analysis of the TPL mandibles by Shackelford and co-authors[37], TPL 3 showed affinities to Pleistocene archaic humans (e.g., non-*H. sapiens* Middle Pleistocene hominins and Neanderthals from Africa and Eurasia), plotting outside of the range of variation of early and Upper Paleolithic *H. sapiens*. This is mainly due to its large bi-mental breadth, an archaic feature also found in early *H. sapien*s and Neanderthals and associated with a wide ramus[60]. However, like other Late Pleistocene *H. sapiens*, TPL 3 has a well-developed chin (mental osseum rank 5[37]), a trademark of our species.

An obvious comparison to TPL 3 is the Zhiren 3 mandibular corpus, potentially an even older hominin dated to over 100 kyr[27–29] although its age has been recently challenged by Sun et al.[30] Zhiren 3 is described as showing a combination of an archaic robust corpus, a modestly developed but clearly modern human-like chin (mental osseum rank 4[61]), and derived dental morphology[23,27]. Overall, this mosaic morphology has been interpreted as representing substantial admixture between dispersing early *H. sapiens* populations from Africa and gene flow into local archaic populations. In our shape analysis on the anterior symphysis there is considerable overlap between Neanderthals and *H. sapiens*; however, *H. erectus*, Liang Bua 1, and Xiahe have a distinct shape. Zhiren 3 is more archaic than TPL 3, and both are less archaic than Xiahe, which is very robust, lacks a chin, and has a receding symphysis[62]. Neither TPL 3 nor Zhiren 3's shapes suggest any special affinities to Denisovans. Zhiren 3 has a short anterior corpus height that is moderately robust, like both TPL mandibles and similar to similar to Zhoukoudian UC 104. The morphologies of both TPL 3 and Zhiren 3 are similar to the mosaic morphology of the earliest *H. sapiens* from Africa[60,63]. Zhiren 3's nearest neighbors according to inter-individual Procrustes distances are primarily Late Pleistocene (Minatogawa A, Zhoukoudian Upper Cave 104, Tam Pong 1) and early *H. sapiens* (Border Cave 2) fossils, and it is small like Minatogawa A, TPL 2, Border Cave 2, and Klasies River Mouth. If the chronology is correct, then Zhiren 3 could be an example of an early dispersal of *H. sapiens* that was unsuccessful. Alternatively, if the geological age is overestimated it could also be an example of one of the earliest inhabitants from a late dispersal, like the TPL hominins.

The geologically younger TPL 2 mandible is smaller and in some aspects of shape more modern than TPL 3. Specifically, TPL 3's symphysis is more vertical, and it has a more rectangular anterior dental arcade. However, TPL 2's lateral corpus is robust, even more than the *H. erectus* mean (Supplementary Fig. 15). In our new reconstruction of TPL 2, we adjusted the dental arcade to make it a few millimeters broader (see Methods; Supplementary Fig. 22). While this changes its position in Procrustes space, with our version plotting closer to Late Pleistocene and Holocene *H. sapiens*, it does not change the overall results. TPL 2 is clearly *H. sapiens*.

TPL 2 is among the smallest mandibles in our study, only larger than the diminutive “Hobbit” fossil Liang Bua 1. The reconstructed TPL 2 mandible shape is most similar to young adult females from the site of Tam Hang in northern Laos[64]. Like their mandibles, the body size estimates for these individuals are small according to a western standard (140–153 cm)[37], comparable to individuals from the site of Minatogawa, Japan[58] and consistent with Holocene humans from East and Southeast Asia[64]. Among living and recent populations, many of the shortest-statured populations are from tropical forest environments[65]. A stable isotope study on snail shells collected from Tam Pà Ling suggests that the environmental conditions during MIS 4 and 3 was similar to the humid climate and forested conditions of Northern Laos today[66]. In the time interval 70 – 33 kyr (TPLOSL-4 and TPLOSL-10)[37], the carbon isotope composition (δ13C values) of mammalian teeth from TPL describes a forested habitat, with significant closed-canopy forests[67]. This is consistent with the environmental reconstruction of TPL based on snails[66] and with the assumption of the return of more forested conditions in the mid-Late Pleistocene[68]. Moreover, the δ13Cdiet values from two teeth of TPL 1 clearly highlights a strict reliance on dietary resources from a forest environment[67].

The TPL1 cranial material was found in the same stratigraphic unit as TPL 2 belonging to the same chronological time frame of 52 – 40 kyr and resembles other Late Pleistocene fossils from Asia. Its frontal shape is most similar to Zhoukoudian Upper Cave 101 and Tabon, a Late Pleistocene fossil from the Palawan Islands in the Philippines dated to around 40 kyr[69,70]. Like Zhoukoudian 101 and Tabon, its frontal bone is robust with a projecting glabella and medial brow ridge and like Liujiang it has a tall and projecting lower maxilla with a broad and deep palate. Previous studies on Zhoukoudian Upper Cave 101 and 103 demonstrate morphological similarities with Upper Paleolithic Europeans and early *H. sapiens* from Africa and the Levant[71,72]. Features like greater supraorbital development including inflated glabella, more pronounced superciliary ridges and depressed nasion, as well as maxillary prognathism, can be generally interpreted as a retention of ancestral morphology rather than admixture with local archaic populations[73].

Tam Pà Ling provides unique insight to human variability and temporal trends in the Late Pleistocene Southeast Asian fossil record, a time and region where hominin fossils are scarce. Since initial excavations in 2009 when a partial cranium was unearthed (TPL 1), a handful of hominin fossils have been discovered at this site indicating human occupation between 86 to 44 kyr. These fossils represent some of the oldest diagnosable *H. sapiens* cranio-mandibular remains in Southeast Asia. The TPL 6 frontal, described here for the first time, provides direct evidence of an early, possibly unsuccessful, dispersal from Africa or the Near East towards Southeast Asia by 70 ± 3 kyr. TPL 6 is remarkably gracile implying that it descended from a gracile immigrant population and not the outcome of local evolution from, or admixture with, *H. erectus* or Denisovans. Our semilandmark geometric shape analyses of the other cranio-mandibular fossils from Tam Pà Ling (TPL 1, 2, and 3) are consistent with previous studies attributing them to *H. sapiens*, and their considerable shape and size variability suggests that high levels of heterogeneity characterize Late Pleistocene modern human groups. Together with the recent local discovery of a Denisovan molar in northern Laos[74], as well as fossils attributed to *H. erectus*[75], *H. floresiensis*[76]and *H. luzonensis*[77], Southeast Asia is proving to be a region that was rich in *Homo* diversity in the Middle to Late Pleistocene.

Methods

Dating of burial sediments

Luminescence dating strategy and methods

To constrain the stratigraphically deepest fossils recovered so far, the partial frontal bone (TPL6) and fragment of a tibia shaft (TPL7), sediment samples for luminescence dating (TPL12-15) were collected directly above and below the fossils (Stratigraphic section Fig. 3). These samples lie around ~ 2 m deeper than the previously deepest sample TPL10[37], and should therefore extend the chronology for the site beyond 70 kyr. From previous experience of the sediments at the site, the quartz beyond a depth of ~ 3m is already saturated and unusable, so we focused on feldspar dating using pIR-IRSL techniques. These techniques provide the best opportunity to extend the TPL sediment chronology to the lower levels of the excavation (> 4.5- 5 m). This is due to the higher dose saturation of feldspars in these high dose rate environments, which increases with depth. Previous feldspar ages have relied on single-aliquots to establish a maximum age but without a source of independent age estimates the extent to which the averaging effect, associated with single-aliquots, had overinflated the age could not be estimated. Therefore, we investigated both single aliquot and single grain feldspar techniques to test this influence on the age estimates, and to establish ages that are comparable in precision to the quartz chronology of the upper levels. After the successful application of single-aliquot feldspar techniques to these sediments[37] and single grain techniques to the nearby Tam Ngu Hao 2 sediments[74], we assumed that a similar success would be achieved. However, the single-grain technique produced very few decays (< 0.1% acceptance rate), which was not feasible with the sample size. This was combined with a limited number of acceptable single-aliquot decays, so we also investigated the use of poly-mineral fine-grained dating techniques. Opaque PVC pipes were hammered into the baulks of the sedimentary sections (see Stratigraphic section Fig. 3 for locations, laboratory codes TPLOSL12-15) and separate bags of sediment from a 30 cm radius around the tubes was collected for dosimetry measurements and water content estimations.

pIR-IRSL single-grain techniques - The single-aliquot techniques are outlined in detail in Shackelford et al.[37] but will be briefly summarized here. Potassium feldspar grains of 90–125 um were separated using standard purification procedures, including a final etch in 10% for 10 mins, to remove the external alpha-dosed rinds[78]. We adopted a post-IR-IRSL procedure for a few hundred feldspars grains loaded onto stainless steel single-aliquot discs and measured in a TL-DA-20 Risø unit containing a DASH setup (Dual Attachment stimulation head). Each aliquot was stimulated for 100 s using infrared (875 nm) light emitting diodes (LEDs) and the emissions were detected using an Electron Tubes Ltd 9235B photomultiplier tube fitted with Schott BG-39 and Corning 7–59 filters to transmit wavelengths of 320–480 nm. We used the same measurement procedures (270°C stimulation and 300°C preheat combination) as determined by the testing conducted by Shackelford et al.[37] on feldspars from a similar depth. The initial IRSL signal measured at 50°C (IR_{50}) and the elevated pIR-IRSL signal measured at 270°C ($pIR\text{-}IRSL_{270}$) was derived from the first 15 s minus the final 50 s of each 250 s IRSL shinedown. We did not apply corrections according to the results of residual dose estimation as the residuals were measured at < 10 Gy, but did apply fading corrections according to Lamothe et al.[79] using a weighted mean fading rate of 1.2 ± 0.2% per decade.

Poly-mineral fine-grained techniques - According to the procedures outlined in Aitken[45] the carbonates and organic material were removed from the raw sediment samples by treating with a 10% dilution of hydrochloric acid, followed by hydrogen peroxide. The chemically treated sediment was then suspended in a 20 cm column of 0.01 N sodium oxalate to disperse for 20 min according to Stokes Law to remove the > 11 mm fraction. This procedure was then repeated for longer 4 h periods to isolate the desired 4–11 µm polymineral fraction. Dispensing 1 mg of this fraction, it was then suspended in small tubes filled with acetone standing on each 10 mm diameter stainless steel disc. The discs were then run in the same equipment setup and procedures as described above.

Dosimetry - To determine the environmental dose (from ^{238}U, ^{235}U, ^{232}Th, and their decay products, and ^{40}K) of samples TPL12-15, we estimated the beta contribution using a Geiger-Muller multi-counter for beta counting of dried and powdered sediment samples in the laboratory allowing for the effects of sample moisture, grain size[80] and HF etching on the attenuation of the beta dose. The U and Th gamma contribution was estimated using thick source alpha counting (using Daybreak 583 thick source alpha counters), while the difference between beta and alpha counting was used to estimate the gamma contribution from potassium. This was supported by high resolution gamma spectrometry of dry and powdered samples (TPL14 and 15) to investigate the entire U and Th decay chains and check for disequilibrium in the cave environment. The cosmic dose contribution was estimated by taking account of the burial depth of the sample (between 6–7 m), the thickness of the cave roof overhead (50 m), the zenith-angle dependence of cosmic rays, and the latitude, longitude, and altitude of the site[81]. Water content was estimated at between 25–30 ± 5% using wet weight/dry weight percentages and saturation tests. This is higher than the other samples in the section due to the increased water availability at depths > 5 m. The corresponding (dry) beta and gamma dose rates were obtained using the conversion factors of Guerin et al.[82], with an internal beta dose rate of 0.72 Gy/kyr^{-1} (due to the radioactive decay of ^{40}K and ^{87}Rb), which were made assuming K (13 ± 1%[83]) and Rb (400 ± 100 $\mu g\ g^{-1}$ [84]) concentrations. For the poly-mineral fine grain dosimetry, the alpha dose was calculated using an alpha efficiency value of 0.10 ± 0.02 according to Schmidt et al[85]. No corrections for beta or alpha attenuation were made due their negligible effects on 4–11 grains[45].

Direct dating of mammalian teeth

By the end of fieldwork 2017, several teeth of large mammals were found associated with the recently found human fossil TPL 6. Among them, two caprine fossil teeth excavated from Tam Pà Ling were exported for coupled US-ESR and U-series direct dating (TPL-

73 and TPL-74). The two molars were collected in 2017 and recovered from the second trench at a depth of 6.40 m and 6.67 m, respectively (Stratigraphic section Fig. 3).

U-series

Teeth were sectioned to expose the different dental tissues using a large diamond blade-rotating saw with a thickness of 350 µm (Direct dating of the fossils Fig. 4) and polished to ~ 50 µm smoothness. Each section was then analyzed by LA-ICPMS quadrupole for uranium distribution and then using an ESI NW193 ArF Excimer laser coupled to a MC-ICPMS Neptune Plus at the University of Wollongong (configuration: jet sample Ni 83506 and x skimmer Ni 76250). The instrument was tuned with the NIST610 at 60% laser energy (2.49 J/cm2), 5Hz, 65 um, 5 m/sec, He: 900 ml/min, N2: 10 ml/min with obtained value of 238U = 1.28V (232Th = 1.05V). Each sample was pre-ablated at 40% laser energy (3.3 J/cm2), 5 Hz, 150 m, 200 um/sec, before conducting measurements of 310m rasters at 80% laser energy (6.27 J/cm2), 20 Hz, 150 m, 5 um/sec.

Between 8 and 11 rasters were drawn on TPL-01 and TPL-02 teeth, respectively, perpendicular to the growth axis of the tooth (from enamel tip to the pulp cavity). Each raster was analyzed twice consecutively and averaged to obtain U-series data. Each average raster represents one distinct minimum U-series age calculation using IsoplotR[86]. Ages were not calculated when U concentration was below 1ppm or when U/Th ratio was below 500. Using the rasters sequence along the growth axis, a modeled U-series age was calculated using a Diffusion-Adsorption-Decay (DAD) model[42] for both TPL-01 and TPL-02 samples. Baseline and drifts were corrected using a NIST 612 glass disc, while two coral standards (the MIS7 Faviid and MIS5 Porites corals from the Southern Cook Islands[87]) were used to correct 234U/238U and 230Th/238U ratios and assess the accuracy of measurements. Each coral standard was analyzed by solution MC-ICPMS at UOW and used for reference. To account for potential matrix effects, a bovid tooth fragment from South Africa with known isotope concentrations was used to verify measurements. To account for tailing effects, measurements were carried out at half-masses of 229.5 and 230.5 for 230Th and 233.5 and 234.5 for 234U[88]. Results are presented in Tables 1 and 2.

US-ESR

Using a hand-held diamond saw following the protocol developed by Grün et al.[89], a piece of enamel was tentatively separated from each tooth. Unfortunately, teeth offered only thin fragile enamel plates and only TPL-02 offered a suitable fragment that remained intact for ESR measurements. After being cleaned of any remaining dentine and cut to the right dimension, TPL-02 fragment was stripped of the outer 100 microns ± 10% on each side using a polishing diamond blade. The enamel fragment was mounted into a parafilm mold within a sample holder to record the angular dependency in the ESR response[43,90]. Fragments were then measured at room temperature on a Freiberg MS5000 ESR X-band spectrometer at a 0.1mT modulation amplitude, 5 scans, 2mW power, 100G sweep, and 100KHz modulation frequency for ESR dating. Irradiation was performed with the Freiberg X-ray irradiation chamber, which contains a Varian VF50 X-ray gun at a voltage of 40KV and 1mA current on the fragment exposed to X-rays without shielding (apart from a 200-micron Al foil layer). The enamel fragment was irradiated, following exponentially increasing irradiation times at 90s, 360s, 900s, 1800s, 3605s and 7200s, the energy output of the X-ray gun is recorded at the beginning and end of each irradiation step and averaged, to calculate the dose rates at each step (average of 0.378 Gy/s). Systematically, the fragment was measured over 180° in x, y and z-configurations with a 20° step[43,90]. ESR intensities were extracted from T_1-B_2 peak-to-peak amplitudes on the merged ESR signal. Isotropic and baseline corrections were applied uniformly across the measured spectra[91]. The amount of NOCORs was estimated at 17% using the protocol described by Joannes-Boyau[43]. The ESR dose response curves were obtained by using merged ESR intensities and associated standard deviations from the repeated measurements (5 accumulations per angle).

Fitting procedures were carried out with the MCDOSE 2.0 software using a Markov Chain Monte Carlo (MCMC) approach based on the Metropolis-Hastings algorithm[92] (see Fig. 4). DE values were obtained by fitting a single saturating exponential (SSE) following the recommendations of Duval and Grün[93]. The internal dose rate was calculated using measurements obtained for U-series age calculation. Concentration and isotopic ratio for the enamel and dentine were averaged to obtain one value for the entire tooth. Equilibrium of the decay chain after 230Th in both dental tissues was assumed. Water content in the enamel and the dentine were assumed at 3% ±1 and 10% ±5. The external dose rate values for water content and elemental content in the sediment were extracted from measurements done on collected sediments from the cave. Gamma dose rate of 1293 mGy ± 116 and sediment content for U, Th and K of 6.02 ppm, 1.03 ppm and 0.87% respectively were calculated from high-resolution gamma spectroscopy obtained on sediment samples collected near the tooth. Cosmic dose rate of 120 mGy ± 13 was used to calculate the total external contribution to the sample. US-ESR ages were modeled using the program by Shao et al.[94], and updated dose rate conversion factors of Guérin et al.[82].

Bayesian modeling of the entire sequence

To evaluate the uncertainties of the dating approach to the entire sequence at Tam Pà Ling, Bayesian modeling was performed on all independent age estimates (33 in total) using the OxCal (version 4.4) software[95] (available at https://c14.arch.ox.ac.uk/oxcal.html). The analyses incorporated the probability distributions of individual ages, constraints imposed by stratigraphic relationships and the reported minimum or maximum nature of some of the individual age estimates. Each individual age was included as a Gaussian distribution (with mean and s.d. defined by the age estimate and their associated uncertainties), and the resulting age ranges for each unit were presented at 1 σ.

Geometric Morphometric Analysis

The fossil sample is comprised of Early, Middle, and Late Pleistocene hominins from Asia, including specimens attributed to *H. erectus*, *H. floresiensis*, *H. sapiens*, and Denisova (Xiahe mandible), Middle to Late Pleistocene African and Near Eastern early *H. sapiens*, and Eurasian Neanderthals. As the taxonomy of the Asian Middle Pleistocene hominins is contested, we have refrained from assigning specimens from this period to a taxon but refer to them as Middle Pleistocene hominins (MPhs). See Supplementary Table 8 for a list of the specimens, their group affiliation, and the landmark dataset they were used in. The Holocene human sample consists of individuals from the sites of Tam Hang South and North, and Tam Nang An, located in Laos, as well as several sites in Vietnam (Cau Giat, Da But, Dong Thuoc, Lang Bon, Lang Cuom, and Long Gao). All specimens are adults based on dental eruption and spheno-occipital fusion.

Data acquisition

Three-dimensional (3D) surface models of each specimen were created from either computed tomography (CT) scans using Avizo v. 7.1 (FEI Visualization Sciences Group, Hillsboro), NextEngine laser scans, or photogrammetry. For further details on the latter method and error tests between these methods see Bergmann et al.[60]. For most fossils, surface models were generated from the original specimen, however when surface models from the original specimen were not available research quality casts were used[60,63,96–98].

Virtual reconstruction

Minor virtual reconstruction was needed for most specimens and performed in either Geomagic Studio 2014 v. 3.0 (Geomagic Inc., Rockhill) or Avizo v. 7.1. The type of reconstruction varied considerably depending on the specimen, but generally included the filling of cracks or holes, removal of sediments, smoothing abraded areas and refitting of fragments. For some fossils in which one side was missing or deformed, bilateral symmetry was exploited by mirror-imaging. Specific details regarding the reconstruction techniques and error tests have been published in Freidline et al.[96–98] and Bergmann et al.[60,63]. Virtual reconstructions were also performed on the Tam Pà Ling specimens 1, 2, and 6. The TPL 3 mandible preserves the anterior mandibular corpus including the alveolus from the right first molar to the left third premolar. Apart from smoothing the surface and filling small holes, no virtual reconstruction was done to this specimen. We describe the virtual reconstruction of TPL 2 and 6 here. The descriptions of the other TPL fossils can be found in the Supplementary Figs. 20–21. The TPL 2 mandible is largely complete (Supplementary Fig. 22), although it is broken at the midline symphysis and is missing the left and right mandibular condyles and the right coronoid process. The complete coronoid process on the left side was mirror-imaged and aligned to the incomplete coronoid process on the right side. In a previous study[39] the right and left halves were rejoined in the symphyseal plane. However, damage to the alveolar bone in this region allows for an alternative reconstruction by slightly broadening the anterior dental arcade to better accommodate the anterior dentition. To do so, geometric morphometric methods were applied to identify an appropriate reference, a similarly small mandible with small anterior dentition. To identify a good reference, we created a landmark and semilandmark hemimandible dataset based on the more complete left side of the TPL 2 mandible. We processed this data according to standard geometric morphometric protocols (e.g., generalized Procrustes analysis *see below*) and used the aligned Procrustes coordinates to identify which specimen it is most similar to according to Procrustes distances. Its nearest neighbor, Tam Hang South 10, a Holocene *H. sapiens* from Laos was then used as a reference to align the left and right sides of the TPL 2 mandible (Supplementary Fig. 22). The TPL 6 frontal consists of a left superciliary arch and supraorbital margin, and portions of the left side of the frontal squama and temporal line (Fig. 1). On the endocranial surface, the left orbital plate is preserved as well as some of the frontal crest. To create a more complete frontal bone, the entire left side was mirror-imaged, creating a right side and aligned to the left side along the frontal crest (Supplementary Figs. 23–24). Three different reconstructions of TPL 6 were made: reconstruction 1 – a simple reflection mirror image along the midsagittal plane, and reconstruction 2 and 3 – rotating the frontal a few millimeters antero-inferiorly. Reconstruction 1 has the most projecting lateral brow ridge and reconstruction 2 the widest frontal bone (Supplementary Fig. 24). To keep the two halves in correct anatomical positions, all reconstructions were aligned along the frontal crest.

Data analysis

Geometric morphometric methods were used to analyze the shape and size of the TPL fossils in a comparative context. Separate landmark datasets (Supplementary Fig. 25, Supplementary Table 9) were created according to the preserved anatomical elements of the TPL cranial and mandibular sample: 1) a frontal dataset, consisting of 118 (semi)landmarks, based on the preserved morphology of TPL 6 and including the TPL 1 frontal; 2) a maxillary dataset according to the TPL 1 maxilla consisting of 94 (semi)landmarks; 3) a mandible dataset based on the more complete TPL 2 mandible, consisting of 474 (semi)landmarks; and 4) a mandibular anterior corpus dataset based on TPL 3, consisting of 133 (semi)landmarks, which also includes TPL 2. 3D coordinates of anatomical landmarks and curve semilandmarks were digitized on the surface models using Landmark Editor[99]. Landmark and semilandmark data were processed and analyzed in RStudio v. 1.4.1717[100] using the "Morpho" package v. 2.9[101] and "geomorph" v. 4.0.2[102,103]. For each dataset, missing bilateral landmarks and semilandmarks were estimated by mirroring the preserved side. Missing landmarks and semilandmarks lacking a bilateral counterpart were estimated by deforming the sample average onto the deficient configuration using thin-plate spline interpolation[96–98, 104]. Curve and surface semilandmarks were slid by minimizing the bending energy of a thin-plate spline deformation between each specimen and the sample mean shape[105,106]. After sliding, all landmarks and semilandmarks datasets were symmetrized and converted to shape variables using a generalized Procrustes analysis[107].

For each dataset, the Procrustes coordinates were analyzed in principal component analyses (PCA) in shape space, and nearest neighbors were calculated according to inter-individual Procrustes distances. The TPL fossils were projected into this PCA space. Shape changes were visualized along PC 1 and PC 2 by warping the sample mean shape along the positive and negative ends of PC 1 and PC 2, plus/minus two standard deviations from the sample mean. To evaluate temporal trends in facial and mandibular shape and to better discriminate between archaic versus modern morphology, mean shapes were calculated for each group (e.g., *H. erectus*, Neanderthal, and early, Late and Holocene *H. sapiens*) in each data set and compared to the TPL fossils. Temporal trends in size were evaluated by calculating the natural logarithm of centroid size for each specimen for each data set and compared across groups. To explore the effect of size on shape (i.e., allometry) we performed multivariate regression analysis by regressing the natural logarithm of centroid size on all Procrustes shape coordinates for each data set. PCAs, between-group PCAs (bgPCA), and cross-validated linear discriminant analyses (CV LDA) were also performed on only the *H. sapiens* sample to evaluate group integrity and to assess taxonomic predictions. In the bgPCA, *H. sapiens* were divided into three groups: early, Late, and Holocene, and the TPL hominins were projected *a posteriori*. The same groupings were used for the CV LDA. Both analyses were conducted using the first few principal components explaining approximately 80% of the total shape variance. All analyses were performed in RStudio v. 1.4.1717[100] primarily using the packages "Morpho" v. 2.9[101] and "geomorph" v. 4.0.2[102,103].

Declarations

Acknowledgements

We thank the Ministry of Information, Culture and Tourism of Laos PDR for encouraging and supporting our work, marking 20 years of collaboration. We thank the authorities of Xon district, Hua Pan Province and the villagers of Long Gua Pa village for their continuous support of our numerous fieldworks.

K.E.W is supported by the Australian Research Council (ARC) with a Discovery grant (DP170101597). L.S. was supported by the National Geographic Society (NGS-399R-18). Additional funding has been provided by several laboratories in France (UMR7206, MNHN (F.D.)/University Paris Diderot/Sorbonne Paris Cité; FRE2029/UMR8045 Babel CNRS/Université de Paris (A-M.B.); Université de Strasbourg, (Ph.D.) and the Department of Human Evolution, Max Planck Institute for Evolutionary Anthropology, Leipzig, Germany (S.E.F and J-J.H.). Warm thanks to Sodipram company, France, for its continuous financial support all these years (F.D.). We thank the following scientists, institutions, curators and museums for attending the excavations or for providing access to fossil and recent humans: Nguyen Anh Tuan, Nguyen Thi Mai Huong, Patrick Semal, Institut royal des Sciences naturelles de Belgique, Brussels; Collections d'anthropologie, MNHN-Musée de l'Homme, Paris, Philippe Mennecier, Serge Bahuchet, Aurelie Fort, Antoine Balzeau, Martin Friess, Muséum national d'histoire naturelle, Paris; Roberto Macchiarelli, Didier Berthet, Arnaud Mazurier, Musée des Confluences, Lyon; Montserrat Sanz, Joan Daura, Antonio Rosas, Museo Nacional de Ciencias Naturales, Madrid; Mauro Rubini, Anthropological Service of S.A.B.A.P.-RM-MET, Rome; Daniel E. Lieberman, Michèle Morgan, Katherine Meyers (Associate Archivist), Peabody Museum of Archeology and Ethnology, Harvard; Israel Hershkovitz, Baruch Arensburg, Sackler School of Medicine, Tel Aviv University; Rockefeller Museum Jerusalem; Abdelouahed Ben-Ncer & Mohammed Abdeljalil El Hajraoui & Samir Raoui, Institut National des Sciences du Patrimoine et de l'Archeólogie and "Direction du Patrimoine Culturel", Rabat; Wendy Black, Miss Erica Bartnick, Iziko Museums of South Africa, Kapstadt; Bernhard Zipfel, Medical School of the University of the Witwatersrand, Johannesburg; and Dongju Zhang, College of Earth Environmental Sciences, Lanzhou University. We thank Prof. C. Marsault and I. Laurenson for providing us with scanner facilities (Radiology Department, Hopital Tenon, Paris), and David Plotzki, Heiko Temming, and Andreas Wintzer (technicians) from the Max Planck Institute of Evolutionary Anthropology for assistance with CT scanning and reconstructing computed tomography data.

Author contributions

Conceptualization: S.E.F, F.D., L.S.

Methodology: S.E.F, K.E.W, P.G., I.B., R.J-B, M.M., Ph.D., J-L.P.

Formal analysis: S.E.F., K.E.W., R.J-B

Investigation: S.E.F., K.E.W., R.J-B, M.M., Ph.D., J-L.P.

Writing - original draft: S.E.F., F.D., L.S., R.J-B, M.M., A-M.B., Ph.D., J-L.P.

Writing - review and editing: S.E.F., F.D., L.S., R.J-B, M.M., A-M.B., Ph.D., J-L.P., H.M.C., P.G., J-J., H.

Supervision: F.D., L.S.

Participation to the TPL survey: F.D., Ph.D., JL.P., A.M.B., L.S., N.A-T., N.M-H, E.P-E., F.A., F.C., P.S., D.S., S.B., Q.B., N.B., A.Z., T.E.D., E.S., S.F.

Project administration: F.D., A.M.B., L.S., V.S., T.L.

Funding acquisition: F.D., J.-J.H., L.S., and contribution of laboratories (K.E.W., R.J-B, M.M, A.M.B., Ph.D.)

Competing interests:

The authors declare no competing interests.

References

1. Mallick, S. *et al.* The Simons Genome Diversity Project: 300 genomes from 142 diverse populations. Nature **538**, 201–206, doi:10.1038/nature18964 (2016).
2. Hublin, J. J. *et al.* New fossils from Jebel Irhoud, Morocco and the pan-African origin of Homo sapiens. Nature **546**, 289–292, doi:10.1038/nature22336 (2017).
3. Groucutt, H. S. *et al.* Rethinking the dispersal of Homo sapiens out of Africa. Evol Anthropol **24**, 149–164, doi:10.1002/evan.21455 (2015).
4. Bae, C. J., Douka, K. & Petraglia, M. D. On the origin of modern humans: Asian perspectives. Science **358**, doi:10.1126/science.aai9067 (2017).
5. Reyes-Centeno, H. Out of Africa and into Asia: Fossil and genetic evidence on modern human origins and dispersals. Quaternary International **416**, 249–262, doi:https://doi.org/10.1016/j.quaint.2015.11.063 (2016).
6. Hublin, J.-J. How old are the oldest *Homo sapiens* in Far East Asia? *Proceedings of the National Academy of Sciences* **118**, e2101173118, doi:10.1073/pnas.2101173118 (2021).
7. Posth, C. *et al.* Pleistocene Mitochondrial Genomes Suggest a Single Major Dispersal of Non-Africans and a Late Glacial Population Turnover in Europe. Curr Biol **26**, 827–833, doi:10.1016/j.cub.2016.01.037 (2016).

8. Fu, Q. *et al.* A revised timescale for human evolution based on ancient mitochondrial genomes. Curr Biol **23**, 553–559, doi:10.1016/j.cub.2013.02.044 (2013).
9. Pagani, L. *et al.* Genomic analyses inform on migration events during the peopling of Eurasia. Nature **538**, 238–242, doi:10.1038/nature19792 (2016).
10. Reyes-Centeno, H. *et al.* Genomic and cranial phenotype data support multiple modern human dispersals from Africa and a southern route into Asia. Proc Natl Acad Sci U S A **111**, 7248–7253, doi:10.1073/pnas.1323666111 (2014).
11. Rasmussen, M. *et al.* An Aboriginal Australian genome reveals separate human dispersals into Asia. Science **334**, 94–98, doi:10.1126/science.1211177 (2011).
12. Tassi, F. *et al.* Early modern human dispersal from Africa: genomic evidence for multiple waves of migration. Investig Genet **6**, 13, doi:10.1186/s13323-015-0030-2 (2015).
13. Bergstrom, A., Stringer, C., Hajdinjak, M., Scerri, E. M. L. & Skoglund, P. Origins of modern human ancestry. Nature **590**, 229–237, doi:10.1038/s41586-021-03244-5 (2021).
14. Sikora, M. A Genomic View of the Pleistocene Population History of Asia. Current Anthropology **58**, S397-S405, doi:10.1086/694422 (2017).
15. Malaspinas, A. S. *et al.* A genomic history of Aboriginal Australia. Nature **538**, 207–214, doi:10.1038/nature18299 (2016).
16. Mondal, M. *et al.* Genomic analysis of Andamanese provides insights into ancient human migration into Asia and adaptation. Nat Genet **48**, 1066–1070, doi:10.1038/ng.3621 (2016).
17. Fu, Q. *et al.* DNA analysis of an early modern human from Tianyuan Cave, China. Proc Natl Acad Sci U S A **110**, 2223–2227, doi:10.1073/pnas.1221359110 (2013).
18. Lipson, M. & Reich, D. A Working Model of the Deep Relationships of Diverse Modern Human Genetic Lineages Outside of Africa. Molecular Biology and Evolution **34**, 889–902, doi:10.1093/molbev/msw293 (2017).
19. Harvati, K. *et al.* Apidima Cave fossils provide earliest evidence of Homo sapiens in Eurasia. Nature **571**, 500–504, doi:10.1038/s41586-019-1376-z (2019).
20. Hershkovitz, I. *et al.* The earliest modern humans outside Africa. Science **359**, 456–459, doi:10.1126/science.aap8369 (2018).
21. Groucutt, H. S. *et al.* Homo sapiens in Arabia by 85,000 years ago. Nat Ecol Evol **2**, 800–809, doi:10.1038/s41559-018-0518-2 (2018).
22. Liu, W. *et al.* The earliest unequivocally modern humans in southern China. Nature **526**, 696–699, doi:10.1038/nature15696 (2015).
23. Martinón-Torres, M., Wu, X., Bermúdez de Castro, J. M., Xing, S. & Liu, W. Homo sapien sin the Eastern Asian Late Pleistocene. Current Anthropology **58**, S434-S448, doi:10.1086/694449 (2017).
24. Liu, W., Wu, X., Pei, S., Wu, X. & Norton, C. J. Huanglong Cave: A Late Pleistocene human fossil site in Hubei Province, China. Quaternary International **211**, 29–41, doi:10.1016/j.quaint.2009.06.017 (2010).
25. Shen, G. *et al.* Mass spectrometric U-series dating of Huanglong Cave in Hubei Province, Central China: evidence for early presence of modern humans in Eastern Asia. J Hum Evol **65**, 162–167, doi:10.1016/j.jhevol.2013.05.002 (2013).
26. Bae, C. J. *et al.* Modern human teeth from Late Pleistocene Luna Cave (Guangxi, China). Quaternary International **354**, 169–183, doi:10.1016/j.quaint.2014.06.051 (2014).
27. Liu, W. *et al.* Human remains from Zhirendong, South China, and modern human emergence in East Asia. Proc Natl Acad Sci U S A **107**, 19201–19206, doi:10.1073/pnas.1014386107 (2010).
28. Cai, Y. *et al.* The age of human remains and associated fauna from Zhiren Cave in Guangxi, southern China. Quaternary International **434**, 84–91, doi:10.1016/j.quaint.2015.12.088 (2017).
29. Ge, J. *et al.* Climate-influenced cave deposition and human occupation during the Pleistocene in Zhiren Cave, southwest China. Quaternary International **559**, 14–23, doi:https://doi.org/10.1016/j.quaint.2020.01.018 (2020).
30. Sun, X.-f. *et al.* Ancient DNA and multimethod dating confirm the late arrival of anatomically modern humans in southern China. *Proceedings of the National Academy of Sciences* **118**, e2019158118, doi:10.1073/pnas.2019158118 (2021).
31. Higham, T. F. G. & Douka, K. The reliability of late radiocarbon dates from the Paleolithic of southern China. Proc Natl Acad Sci U S A **118**, doi:10.1073/pnas.2103798118 (2021).

32. Martinon-Torres, M. *et al.* On the misidentification and unreliable context of the new "human teeth" from Fuyan Cave (China). Proc Natl Acad Sci U S A **118**, doi:10.1073/pnas.2102961118 (2021).
33. Shen, G. *et al.* U-Series dating of Liujiang hominid site in Guangxi, Southern China. J Hum Evol **43**, 817–829 (2002).
34. Wu, X. & Poirier, F. E. *Human Evolution in China*. (Oxford University Press, 1995).
35. Westaway, K. E. *et al.* An early modern human presence in Sumatra 73,000–63,000 years ago. Nature **548**, 322–325, doi:10.1038/nature23452 (2017).
36. Demeter, F. *et al.* Anatomically modern human in Southeast Asia (Laos) by 46 ka. Proc Natl Acad Sci U S A **109**, 14375–14380, doi:10.1073/pnas.1208104109 (2012).
37. Shackelford, L. *et al.* Additional evidence for early modern human morphological diversity in Southeast Asia at Tam Pa Ling, Laos. Quaternary International **466**, 93–106, doi:10.1016/j.quaint.2016.12.002 (2018).
38. Clarkson, C. *et al.* Human occupation of northern Australia by 65,000 years ago. Nature **547**, 306–310, doi:10.1038/nature22968 (2017).
39. Demeter, F. *et al.* Early modern humans and morphological variation in Southeast Asia: fossil evidence from Tam Pa Ling, Laos. PLoS One **10**, e0121193, doi:10.1371/journal.pone.0121193 (2015).
40. Demeter, F. *et al.* Early Modern Humans from Tam Pà Ling, Laos: Fossil Review and Perspectives. Current Anthropology **58**, S527-S538, doi:10.1086/694192 (2017).
41. Sambridge, M., Grün, R. & Eggins, S. U-series dating of bone in an open system: The diffusion-adsorption-decay model. Quaternary Geochronology **9**, 42–53, doi:https://doi.org/10.1016/j.quageo.2012.02.010 (2012).
42. Grün, R., Eggins, S., Kinsley, L., Moseley, H. & Sambridge, M. Laser ablation U-series analysis of fossil bones and teeth. Palaeogeography, Palaeoclimatology, Palaeoecology **416**, 150–167, doi:https://doi.org/10.1016/j.palaeo.2014.07.023 (2014).
43. Joannes-Boyau, R. Detailed protocol for an accurate non-destructive direct dating of tooth enamel fragment using Electron Spin Resonance. Geochronometria **40**, 322–333, doi:10.2478/s13386-013-0132-7 (2013).
44. Zimmerman, D. W. Thermoluminescent dating using fine grains from pottery. Archaeometry **13**, 29–52, doi:https://doi.org/10.1111/j.1475-4754.1971.tb00028.x (1971).
45. Aitken, M. J. *Thermoluminescence dating*. (Academic Press, 1985).
46. Fu, Q. *et al.* An early modern human from Romania with a recent Neanderthal ancestor. Nature **524**, 216–219, doi:10.1038/nature14558 (2015).
47. Fu, Q. *et al.* Genome sequence of a 45,000-year-old modern human from western Siberia. Nature **514**, 445–449, doi:10.1038/nature13810 (2014).
48. Fu, Q. *et al.* The genetic history of Ice Age Europe. Nature **534**, 200–205, doi:10.1038/nature17993 (2016).
49. Hajdinjak, M. *et al.* Initial Upper Palaeolithic humans in Europe had recent Neanderthal ancestry. Nature **592**, 253–257, doi:10.1038/s41586-021-03335-3 (2021).
50. Seguin-Orlando, A. *et al.* Genomic structure in Europeans dating back at least 36,200 years. Science **346**, 1113–1118, doi:doi:10.1126/science.aaa0114 (2014).
51. Yang, M. A. *et al.* 40,000-Year-Old Individual from Asia Provides Insight into Early Population Structure in Eurasia. Current Biology **27**, 3202–3208.e3209, doi:10.1016/j.cub.2017.09.030 (2017).
52. Lipson, M. *et al.* Ancient genomes document multiple waves of migration in Southeast Asian prehistory. *bioRxiv*, 279646, doi:10.1101/279646 (2018).
53. McColl, H. *et al.* The prehistoric peopling of Southeast Asia. Science **361**, 88–92, doi:doi:10.1126/science.aat3628 (2018).
54. Weidenreich, F. On the earliest representatives of modern mankind recovered on the soil of East Asia. Pek. Nat. Hist. Bul. **13**, 161–174 (1938-39).
55. Cunningham, D. L. & Wescott, D. J. Within-group human variation in the Asian Pleistocene: the three Upper Cave crania. J Hum Evol **42**, 627–638, doi:10.1006/jhev.2001.0547 (2002).
56. Matsu'ura, S. in *Interdisciplinary Perspectives on the Origins of the Japanese* (ed K. Omoto) 118–197 (International Research Center for Japanese Studies, 1999).
57. Kaifu, Y., Fujita, M., Kono, R. T. & Baba, H. Late Pleistocene modern human mandibles from the Minatogawa Fissure site, Okinawa, Japan: morphological affinities and implications for modern human dispersals in East Asia. Anthropological Science **119**, 137–

157, doi:10.1537/ase.090424 (2011).

58. Baba, H. & Narasaki, S. Minatogawa Man, the Oldest Type of Modern < i > Homo sapiens</i > in East Asia. The Quaternary Research (Daiyonki-Kenkyu) **30**, 221–230, doi:10.4116/jaqua.30.221 (1991).
59. Baba, H., Narasaki, S. & Ohyama, S. Minatogawa Hominid Fossils and the Evolution of Late Pleistocene Humans in East Asia. Anthropological Science **106**, 27–45, doi:10.1537/ase.106.Supplement_27 (1998).
60. Bergmann, I., Hublin, J.-J., Gunz, P. & Freidline, S. E. How did modern morphology evolve in the human mandible? The relationship between static adult allometry and mandibular variability in Homo sapiens. Journal of Human Evolution **157**, 103026, doi:https://doi.org/10.1016/j.jhevol.2021.103026 (2021).
61. Dobson, S. D. & Trinkaus, E. Cross-sectional geometry and morphology of the mandibular symphysis in Middle and Late Pleistocene Homo. Journal of Human Evolution **43**, 67–87, doi:https://doi.org/10.1006/jhev.2002.0563 (2002).
62. Chen, F. *et al.* A late Middle Pleistocene Denisovan mandible from the Tibetan Plateau. Nature, doi:10.1038/s41586-019-1139-x (2019).
63. Bergmann, I. *et al.* The relevance of late MSA mandibles on the emergence of modern morphology in Northern Africa. Sci Rep **12**, 8841, doi:10.1038/s41598-022-12607-5 (2022).
64. Shackelford, L. & Demeter, F. The place of Tam Hang in Southeast Asian human evolution. Comptes Rendus Palevol **11**, 97–115, doi:10.1016/j.crpv.2011.07.002 (2012).
65. Klein-Nulend, J. & Bonewald, L. F. in Principles of Bone Biology 133–162 (2020).
66. Milano, S. *et al.* Environmental conditions framing the first evidence of modern humans at Tam Pà Ling, Laos: A stable isotope record from terrestrial gastropod carbonates. Palaeogeography, Palaeoclimatology, Palaeoecology **511**, 352–363, doi:10.1016/j.palaeo.2018.08.020 (2018).
67. Bourgon, N. *et al.* Trophic ecology of a Late Pleistocene early modern human from tropical Southeast Asia inferred from zinc isotopes. J Hum Evol **161**, 103075, doi:10.1016/j.jhevol.2021.103075 (2021).
68. Bacon, A. M. *et al.* A multi-proxy approach to exploring Homo sapiens' arrival, environments and adaptations in Southeast Asia. Sci Rep **11**, 21080, doi:10.1038/s41598-021-99931-4 (2021).
69. Dizon, E. *et al.* Notes on the Morphology and Age of the Tabon Cave Fossil Homo sapiens. Current Anthropology **43**, 660–666, doi:10.1086/342432 (2002).
70. Détroit, F. *et al.* Upper Pleistocene Homo sapiens from the Tabon cave (Palawan, The Philippines): description and dating of new discoveries. Comptes Rendus Palevol **3**, 705–712, doi:10.1016/j.crpv.2004.06.004 (2004).
71. Stringer, C. B. Reconstructing recent human evolution. Philos Trans R Soc Lond B Biol Sci **337**, 217–224 (1992).
72. Harvati, K. Into Eurasia: a geometric morphometric re-assessment of the Upper Cave (Zhoukoudian) specimens. J Hum Evol **57**, 751–762, doi:10.1016/j.jhevol.2009.07.008 (2009).
73. Lahr, M. M. Patterns of modern human diversification: Implications for Amerindian origins. American Journal of Physical Anthropology **38**, 163–198, doi:https://doi.org/10.1002/ajpa.1330380609 (1995).
74. Demeter, F. *et al.* A Middle Pleistocene Denisovan molar from the Annamite Chain of northern Laos. Nat Commun **13**, 2557, doi:10.1038/s41467-022-29923-z (2022).
75. Rizal, Y. *et al.* Last appearance of Homo erectus at Ngandong, Java, 117,000-108,000 years ago. Nature **577**, 381–385, doi:10.1038/s41586-019-1863-2 (2020).
76. Morwood, M. J. *et al.* Further evidence for small-bodied hominins from the Late Pleistocene of Flores, Indonesia. Nature **437**, 1012–1017, doi:10.1038/nature04022 (2005).
77. Detroit, F. *et al.* A new species of Homo from the Late Pleistocene of the Philippines. Nature **568**, 181–186, doi:10.1038/s41586-019-1067-9 (2019).
78. Aitken, M. J. *An introduction to optical dating: the dating of Quaternary sediments by the use of photon-stimulated luminescence*. (Oxford University Press, 1998).
79. Lamothe, M., Auclair, M., Hamzaoui, C. & Huot, S. Towards a prediction of long-term anomalous fading of feldspar IRSL. Radiation Measurements **37**, 493–498, doi:https://doi.org/10.1016/S1350-4487(03)00016-7 (2003).
80. Mejdahl, V. Thermoluminescence dating: beta-dose attenuation in quartz grains. Archaeometry **21**, 61–72 (1979).

81. Prescott, J. R. & Hutton, J. T. Cosmic ray contributions to dose rates for luminescence and ESR dating: Large depths and long-term time variations. Radiation Measurements **23**, 497–500, doi:https://doi.org/10.1016/1350-4487(94)90086-8 (1994).
82. Guérin, G., Mercier, N. & Adamiec, G. Dose-rate conversion factors: Update. Ancient TL **29**, 5–8 (2011).
83. Huntley, D. J. & Baril, M. R. The K content of the K-feldspars being measured in optical dating or in thermoluminescence dating. Ancient TL **15**, 11–13 (1997).
84. Huntley & Hancock, R. The Rb contents of the K-feldspar grains being measured in optical dating. Ancient Tl **19**, 43–46 (2001).
85. Schmidt, C., Bösken, J. & Kolb, T. Is there a common alpha-efficiency in polymineral samples measured by various infrared stimulated luminescence protocols? *Geochronometria* **45**, 160–172, doi:doi:10.1515/geochr-2015-0095 (2018).
86. Vermeesch, P. IsoplotR: A free and open toolbox for geochronology. Geoscience Frontiers **9**, 1479–1493, doi:https://doi.org/10.1016/j.gsf.2018.04.001 (2018).
87. Woodroffe, C. D., Short, S. A., Stoddart, D. R., Spencer, T. & Harmon, R. S. Stratigraphy and chronology of late pleistocene reefs in the Southern Cook Islands, south Pacific. Quaternary Research **35**, 246–263, doi:https://doi.org/10.1016/0033-5894(91)90071-C (1991).
88. Eggins, S., Grün, R., Pike, A. W. G., Shelley, M. & Taylor, L. 238U, 232Th profiling and U-series isotope analysis of fossil teeth by laser ablation-ICPMS. Quaternary Science Reviews **22**, 1373–1382, doi:https://doi.org/10.1016/S0277-3791(03)00064-7 (2003).
89. Grün, R., Aubert, M., Joannes-Boyau, R. & Moncel, M.-H. High resolution analysis of uranium and thorium concentration as well as U-series isotope distributions in a Neanderthal tooth from Payre (Ardèche, France) using laser ablation ICP-MS. Geochimica et Cosmochimica Acta **72**, 5278–5290, doi:https://doi.org/10.1016/j.gca.2008.08.007 (2008).
90. Joannes-Boyau, R. & Grün, R. A comprehensive model for CO2 – radicals in fossil tooth enamel: Implications for ESR dating. Quaternary Geochronology **6**, 82–97, doi:https://doi.org/10.1016/j.quageo.2010.09.001 (2011).
91. Joannes-Boyau, R. & Grün, R. Thermal behavior of orientated and non-orientated CO2 – radicals in tooth enamel. Radiation Measurements **44**, 505–511, doi:https://doi.org/10.1016/j.radmeas.2009.02.010 (2009).
92. Joannes-Boyau, R., Duval, M. & Bodin, T. MCDoseE 2.0 A new Markov Chain Monte Carlo program for ESR dose response curve fitting and dose evaluation. Quaternary Geochronology **44**, 13–22, doi:https://doi.org/10.1016/j.quageo.2017.11.003 (2018).
93. Duval, M. & Grün, R. Are published ESR dose assessments on fossil tooth enamel reliable? Quaternary Geochronology **31**, 19–27, doi:https://doi.org/10.1016/j.quageo.2015.09.007 (2016).
94. Shao, Q., Bahain, J.-J., Dolo, J.-M. & Falguères, C. Monte Carlo approach to calculate US-ESR age and age uncertainty for tooth enamel. Quaternary Geochronology **22**, 99–106, doi:https://doi.org/10.1016/j.quageo.2014.03.003 (2014).
95. Bronk Ramsey, C. Radiocarbon Calibration and Analysis of Stratigraphy: The OxCal Program. Radiocarbon **37**, 425–430, doi:10.1017/S0033822200030903 (1995).
96. Freidline, S. E., Gunz, P., Harvati, K. & Hublin, J.-J. Middle Pleistocene human facial morphology in an evolutionary and developmental context. J Hum Evol **63**, 723–740, doi:10.1016/j.jhevol.2012.08.002 (2012).
97. Freidline, S. E., Gunz, P., Harvati, K. & Hublin, J.-J. Evaluating developmental shape changes in *Homo antecessor* subadult facial morphology. J Hum Evol **65**, 404–423, doi:10.1016/j.jhevol.2013.07.012 (2013).
98. Freidline, S. E., Gunz, P., Janković, I., Harvati, K. & Hublin, J. J. A comprehensive morphometric analysis of the frontal and zygomatic bone of the Zuttiyeh fossil from Israel. J Hum Evol **62**, 225–241, doi:10.1016/j.jhevol.2011.11.005 (2012).
99. Wiley, D. F. *et al*. Evolutionary morphing. *Proceedings of IEEE Visualizations* (2005).
100. Team, R. C. *R: A language and environment for statistical computing*, <https://www.R-project.org/> (2021).
101. Schlager, S. in *Statistical Shape and Deformation Analysis* (ed S. Li G. Zheng, G. Szekely) 217–256 (Academic Press, 2017).
102. Adams, D., Collyer, M., Kaliontzopoulou, A. & Baken, E. *Geomorph: Software for geometric morphometric analyses. R package version 4.0.2*, <https://cran.r-project.org/package=geomorph.> (2021).
103. Baken, E. K., Collyer, M. L., Kaliontzopoulou, A. & Adams, D. C. geomorph v4.0 and gmShiny: Enhanced analytics and a new graphical interface for a comprehensive morphometric experience. Methods in Ecology and Evolution **12**, 2355–2363, doi:https://doi.org/10.1111/2041-210X.13723 (2021).
104. Gunz, P., Mitteroecker, P., Neubauer, S., Weber, G. W. & Bookstein, F. L. Principles for the virtual reconstruction of hominin crania. J Hum Evol **57**, 48–62, doi:10.1016/j.jhevol.2009.04.004 (2009).

105. Gunz, P., Mitteroecker, P. & Bookstein, F. in *Modern Morphometrics in Physical Anthropology* (ed D.E. Slice) 73–98 (Plenum Publishers, 2005).

106. Gunz, P. & Mitteroecker, P. Semilandmarks: a method for quantifying curves and surfaces. Hystrix, the Italian Journal of Mammalogy **24**, 103–109, doi:10.4404/hystrix-24.1-6292 (2013).

107. Rohlf, F. J. & Slice, D. Extensions of the Procrustes Method for the Optimal Superimposition of Landmarks. Systematic Biology **39**, 40–59, doi:10.2307/2992207 (1990).

Tables

Table 1
U-series dating of TPL-01 and TPL-02.

Sample/raster	U (ppm)	U/Th	$^{234}U/^{238}U$	2s	$^{230}Th/^{238}U$	2s	Age	2s
TPL-01								
TPL-01-R1-enamel	-0.1	239	1.2600	0.2000	1.3400	0.5200	-	-
TPL-01-R2-enamel	0.1	-787	1.5170	0.0560	0.6830	0.0820	-	-
TPL-01-R3-dentine	40.5	-675000	1.4643	0.0037	0.6698	0.0089	**64.2**	**1.1**
TPL-01-R4-dentine	44.1	2205000	1.4668	0.0042	0.6810	0.0110	**65.9**	**1.4**
TPL-01-R5-dentine	45.3	75500	1.4650	0.0048	0.6720	0.0092	**64.3**	**1.2**
TPL-01-R6-dentine	49.1	100204	1.4655	0.0047	0.6560	0.0110	**62.0**	**1.4**
TPL-01-R7-dentine	45.5	284	1.4624	0.0047	0.6540	0.0120	-	-
TPL-01-R8-dentine	3.1	1	0.9400	0.0650	1.0540	0.0620	-	-
TPL-02								
TPL-02-R1-dentine	35.9	12379	1.6572	0.0075	0.7660	0.0150	**64.6**	**1.7**
TPL-02-R2-dentine	35.3	28934	1.6528	0.0050	0.7947	0.0099	**68.0**	**1.2**
TPL-02-R3-dentine	35.5	1014	1.6450	0.0120	0.7830	0.0120	**67.1**	**1.5**
TPL-02-R4-dentine	38.3	51067	1.6450	0.0035	0.7944	0.0073	**68.4**	**0.9**
TPL-02-R5-dentine	35.8	85238	1.6467	0.0042	0.7840	0.0120	**67.2**	**1.4**
TPL-02-R6-dentine	34.9	21813	1.6418	0.0049	0.7902	0.0096	**68.1**	**1.1**
TPL-02-R7-enamel	0.2	110	1.5160	0.0500	0.5820	0.0810	-	-
TPL-02-R8-enamel	0.1	133	1.5270	0.0770	0.5570	0.0750	-	-
TPL-02-R9-enamel	0.1	384	1.5430	0.0570	0.6080	0.0750	-	-
TPL-02-R10-enamel	0.0	42	1.5180	0.0870	0.6100	0.1200	-	-
TPL-02-R11-enamel	0.0	-19	1.4800	0.1100	0.8200	0.1200	-	-

Table 2
DAD model results for each sample.

Sample	Mean Age U-series (ka)	Number of rasters	Age DAD (ka)	2s-Error
TPL-01	64.1ka+/-1.3	5	**67**	**+1.8/-2.2**
TPL-02	67.3ka+/-1.3	6	**71**	**+1.5/-1.5**

Table 3: pIR-IRSL coarse grain and polymineral fine-grained dating of sediments at Tam Pa Ling: dose rate data, equivalent doses, and age estimates

A: Alpha and beta counting

Sample	Depth	Gamma	Beta	Cosmic-ray	Int/Alpha	Water	Total	Accepted		Equivalent	
code[a]		dose rate	dose rate	dose rate	dose rate	content	dose rate	/Run	Technique[g]	dose	Age
	(m)	(Gy ka^{-1})[b]	(Gy ka^{-1})[b]	(Gy ka^{-1})[c]	(Gy ka^{-1})[d]	(%)[e]	(Gy ka^{-1})	Aliquots[f]		(Gy)[h,i]	(ka)[i]
TPL12	5.72	1.670 ± 0.080	1.578 ± 0.066	0.013 ± 0.001	0.72 ± 0.10	30 / 30 ± 2	3.982 ± 0.186	13/24	pIR-IRSL$_{270}$	266 ± 14	**67 ± 5**
TPL13	6.00	1.453 ± 0.087	1.206 ± 0.054	0.013 ± 0.001	0.72 ± 0.10	30 / 30 ± 5	3.392 ± 0.209	5/32	pIR-IRSL$_{270}$	240 ± 50	**71 ± 16**
		1.453 ± 0.087	1.327 ± 0.052	0.013 ± 0.001	0.20 ± 0.04	30 / 30 ± 5	2.995 ± 0.179	9/13	PFG	194 ± 57	**65 ± 19**
TPL14	6.30	1.777 ± 0.083	1.623 ± 0.069	0.013 ± 0.001	0.72 ± 0.10	34 / 30 ± 5	4.133 ± 0.236	13/34	pIR-IRSL$_{270}$	307 ± 41	**74 ± 11**
		1.777 ± 0.083	1.786 ± 0.065	0.013 ± 0.001	0.24 ± 0.07	34 / 30 ± 5	3.812 ± 0.200	10/12	PFG	240 ± 44	**63 ± 12**
TPL15	6.67	1.591 ± 0.051	1.588 ± 0.073	0.013 ± 0.001	0.72 ± 0.10	40 / 30 ± 5	3.912 ± 0.212	4/8	pIR-IRSL$_{270}$	313 ± 36	**80 ± 10**
		1.591 ± 0.051	1.747 ± 0.032	0.013 ± 0.001	0.35 ± 0.09	40 / 30 ± 5	3.450 ± 0.190	6/11	PFG	295 ± 20	**86 ± 8**

[a] Samples processed using the 90-125 µm size fraction or poly-mineral fine grains (4-11 µm). Fig. 3 contains the sampling location

[b] Beta dose rates were estimated using a Geiger Muller beta counting of dried and powdered sediment samples, gamma dose rates were estimated using thick source alpha counting measurements of dried and powdered sediment samples in the laboratory. The difference between these measurements was used to estimate potassium values.

[c] Time-averaged cosmic-ray dose rates (for dry samples), each assigned an uncertainty of ± 10%.

[d] An internal dose rate of 0.72 ± 0.10 Gy/ka was estimated for all 90-125 µm feldspar grains. Mean ± total (1σ) uncertainty, calculated as the quadratic sum of the random and systematic uncertainties. For fine grains this column represents the alpha dose rate based on an effective alpha value for poly-mineral fine grains of 0.10 ± 0.01[76]. For all fine-grain dosimetry no attenuation of beta was included[44]

[e] Field / time-averaged water contents, expressed as (mass of water/mass of dry sample) x 100. The latter values were used to correct the external gamma and beta dose rates.

[f] Total number of aliquots processed verses number of accepted aliquots- with an average acceptance rate of ~15-50%

[g] pIR-IRSL270 indicates coarse grain feldspars using 90-125 µm grains, PFG represents a poly-mineral fine grain measurement on small 4-11 µm grains.

[h] Equivalent doses include a ± 2% systematic uncertainty associated with laboratory beta-source calibrations and represents a fading corrected D_e. Fading corrections according to Lamothe et al.[70]

[i] Uncertainties at 68% confidence interval.

B High resolution gamma spectrometry

Sample	^{238}U	^{226}Ra	^{210}Pb	^{228}Ra	^{228}Th	^{40}K	Water	Total		Equivalent	
code[a]							content	dose rate[b]	Technique[c]	dosed[d]	Age[e]
	(Bq/kg)	(Bq/kg)	(Bq/kg)	(Bq/kg)	(Bq/kg)	(Bq/kg)	(%)	(Gy ka^{-1})		(Gy)	(ka)
TPL14	69 ± 11	52.9 ± 4.7	67.5 ± 11.3	86.7 ± 8.4	96.2 ± 9.3	395 ± 54	34 / 30 ± 5	3.868 ± 0.316	pIR-IRSL$_{270}$	307 ± 41	**79 ± 13**
	69 ± 11	52.9 ± 4.7	67.5 ± 11.3	86.7 ±8.4	96.2 ± 9.3	395 ± 54	34 / 30 ± 5	3.537 ± 0.309	PFG	240 ± 44	**68 ± 14**
TPL15	66 ± 10	57.4 ± 5.2	55.9 ± 9.5	93.3 ± 8.4	89.9 ± 9.9	512 ± 59	40 / 30 ± 5	3.891 ± 0.314	pIR-IRSL$_{270}$	313 ± 36	**80 ± 11**
	66 ± 10	57.4 ± 5.2	55.9 ± 9.5	93.3 ± 8.4	89.9 ± 9.9	512 ± 59	40 / 30 ± 5	3.667 ± 0.323	PFG	295 ± 20	**86 ± 8**

[a] High-resolution gamma spectrometry to estimate the U, Th and K concentrations in the dried and powdered sample, provide a comparison of dose rate, and to test the degree of disequilibrium occurring at the site. HRGS was only measured for samples TPL14 and TPL15. All other parameters such as cosmic dose rate, internal dose rate/alpha dose rate and number of aliquots remains the same as Table A.

[b] The total dose rates for for both samples is slightly lower than Table A resulting in a higher age estimate.

[c] pIR-IRSL$_{270}$ indicates coarse grain feldspars using 90-125 μm grains, PFG represents a poly-mineral fine grain measurement on small 4-11 μm grains.

[d] The Equivalent dose represents a fading corrected De. Fading corrections according to Lamothe et al.[70]

[e] The age estimates have been calculated using these alternate dose rate estimations.

Figures

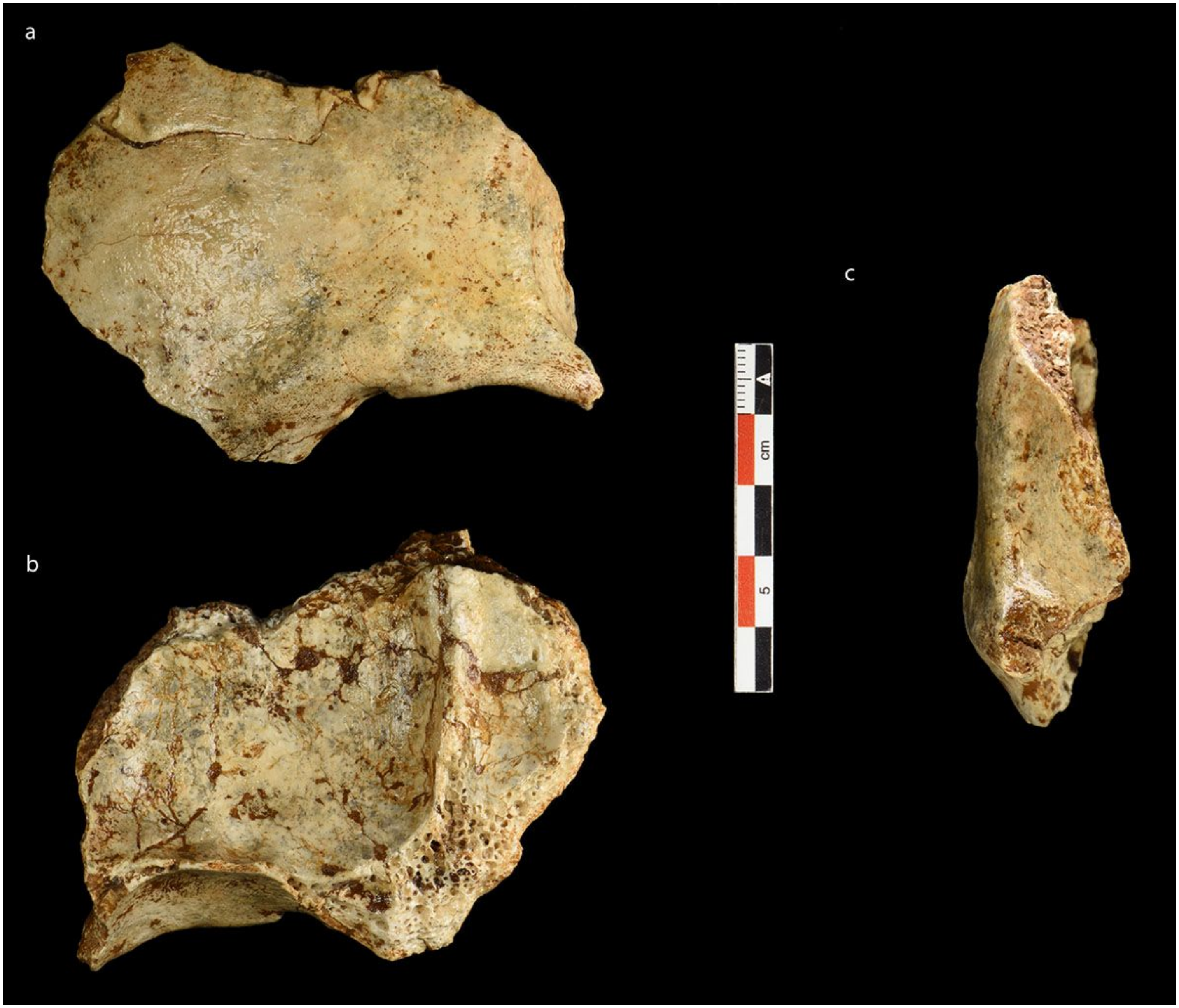

Figure 1

Photograph of the TPL 6 frontal bone. A- anterior view of the left superciliary arch and supraorbital margin, and portions of the frontal squama and temporal line; **B** - endocranial surface including some of the left orbital plate and frontal crest; **C** -lateral view.

Figure 2

Photograph of TPL 7 tibial fragment. A - medial view; **B -** lateral view; **C -** posterior view; **D -** anterior view; **E -** distal view; **F -** proximal view.

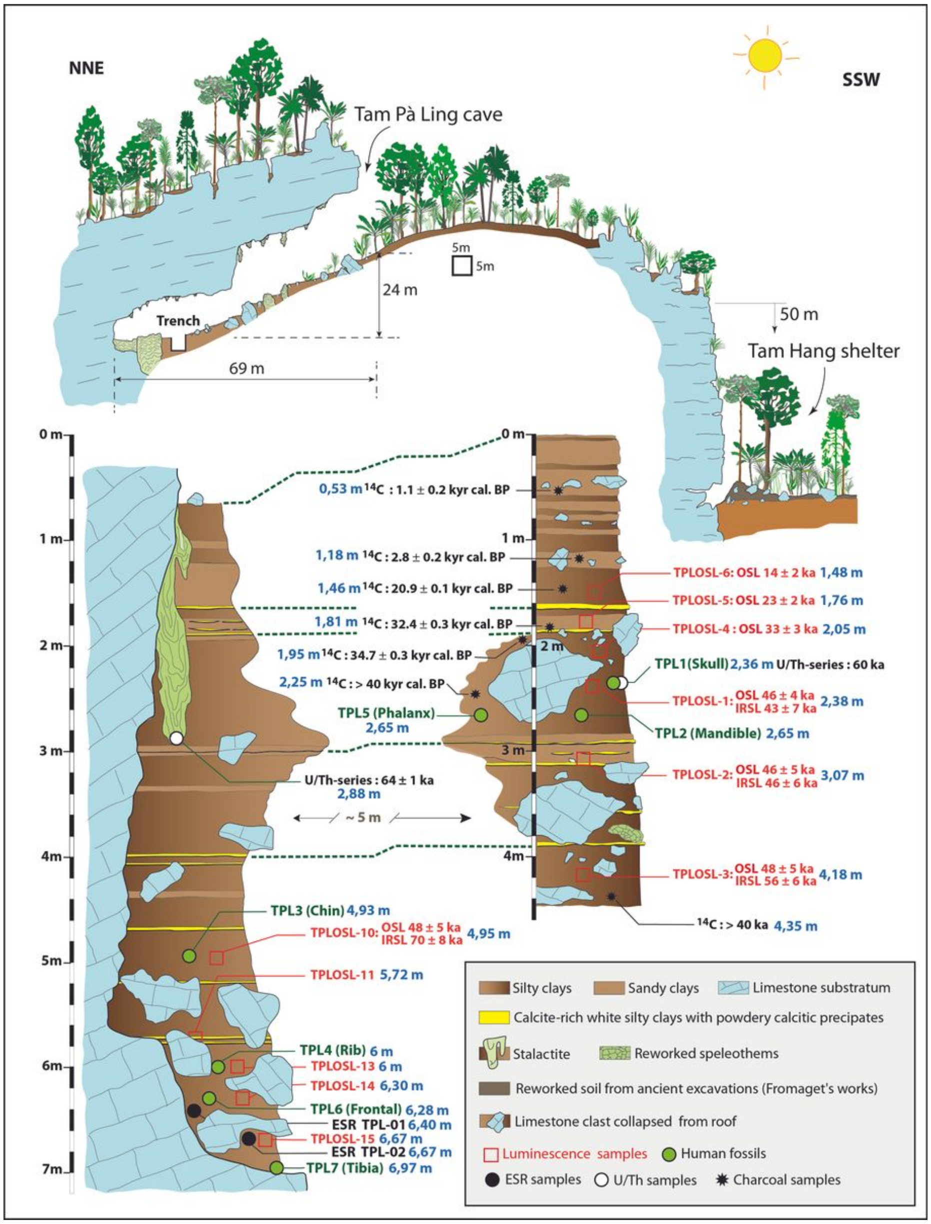

Figure 3

Stratigraphic sections of the main excavation at Tam Pà Ling. Profile 1 on the right is located at the base of the slope directly facing the entrance of the cave, and Profile 2, which is ~5 m adjacent to the cave wall.

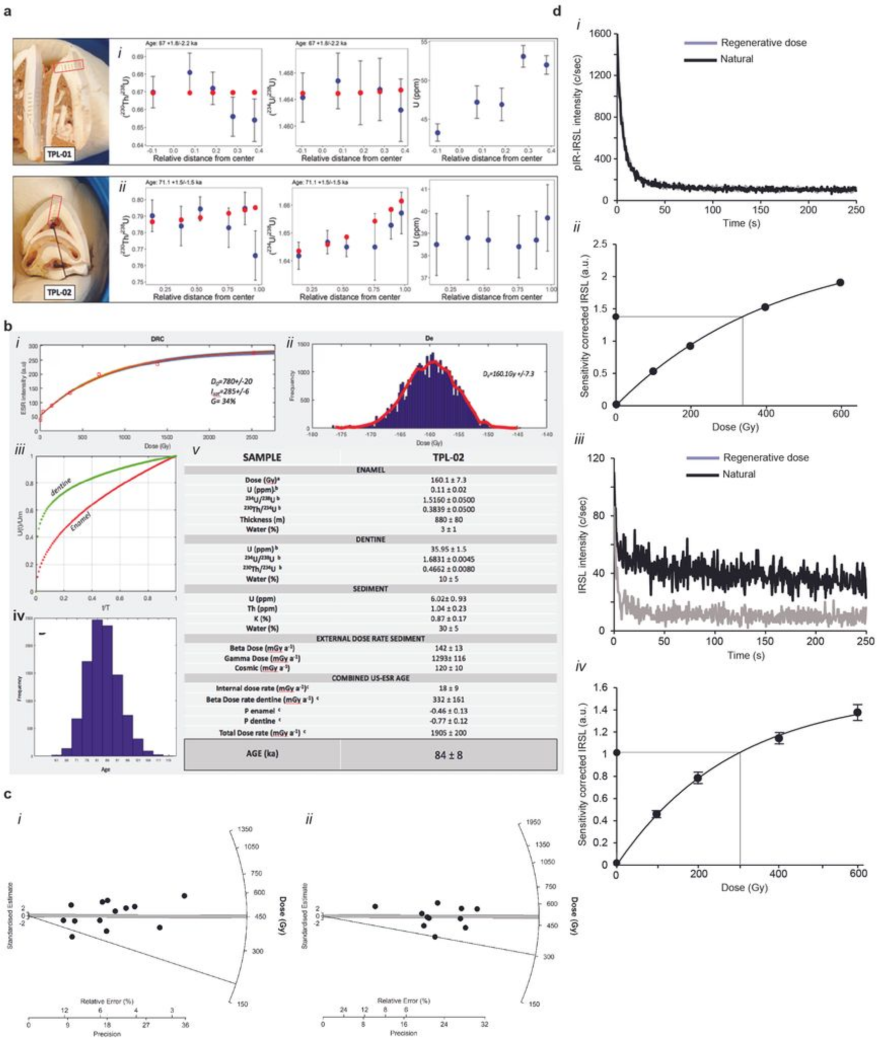

SAMPLE	TPL-02
ENAMEL	
Dose (Gy)[a]	160.1 ± 7.3
U (ppm)[b]	0.11 ± 0.02
$^{234}U/^{238}U$ [b]	1.5160 ± 0.0500
$^{230}Th/^{234}U$ [b]	0.3839 ± 0.0500
Thickness (m)	880 ± 80
Water (%)	3 ± 1
DENTINE	
U (ppm)[b]	35.95 ± 1.5
$^{234}U/^{238}U$ [b]	1.6831 ± 0.0045
$^{230}Th/^{234}U$ [b]	0.4662 ± 0.0080
Water (%)	10 ± 5
SEDIMENT	
U (ppm)	6.02± 0.93
Th (ppm)	1.04 ± 0.23
K (%)	0.87 ± 0.17
Water (%)	30 ± 5
EXTERNAL DOSE RATE SEDIMENT	
Beta Dose (mGy a^{-1})	142 ± 13
Gamma Dose (mGy a^{-1})	1293± 116
Cosmic (mGy a^{-1})	120 ± 10
COMBINED US-ESR AGE	
Internal dose rate (mGy a^{-1})[c]	18 ± 9
Beta Dose rate dentine (mGy a^{-1}) [c]	332 ± 161
P enamel [c]	-0.46 ± 0.13
P dentine [c]	-0.77 ± 0.12
Total Dose rate (mGy a^{-1}) [c]	1905 ± 200
AGE (ka)	84 ± 8

Figure 4

Direct dating of fossil teeth and luminescence dating of sediments. A - (i) Diffusion-Adsorption-Decay (DAD) results for TPL-01 and TPL-02. Upper (from left to right) picture of TPL-01 with indication of LA-MC-ICPMS rasters position; $^{230}Th/^{238}U$ diffusion relative to distance from center, $^{234}U/^{238}U$ diffusion relative to distance from center, and U concentration relative to distance from center. (ii) Lower (from left to right) picture of TPL-02 with indication of LA-MC-ICPMS rasters position; $^{230}Th/^{238}U$ diffusion relative to distance from center, $^{234}U/^{238}U$ diffusion relative to distance from center, and U concentration relative to distance from center. **B** - Summary of the US-ESR results for TPL-02. (i) Distribution of the Dose Response Curve (DRC); (ii) Probabilistic distribution of the equivalent dose; (iii) Diffusion pattern of U in the enamel and dentine over time; (iv) Probabilistic distribution of TPL-02 ages. (v) Table summarizing the US-ESR parameters. (a) dose equivalent D_e obtained using McDoseE 2.0 (Joannes-Boyau et al., 2018); (b) Uranium concentration values were obtained by LA-MC-ICPMS (dentine and enamel values are averaged); (c) Parameters and ages were calculated using Shao et al.[94] and updated values from Guerin et al., 2011[82]. **C -** Luminescence data for sample TPL14, radial plots for (i) pIR-IRSL single aliquot dating of feldspars and (ii) pIR-IRSL poly-mineral fine grained dating. D - Luminescence data for sample TPL14, (i) pIR-IRSL shine down curve and (ii) dose response curve for pIR-IRSL single aliquot of feldspars. The resulting D_e was 337 ± 32 Gy, (iii) pIR-IRSL shine down curve and (ii) dose response curve for poly-mineral fine grains, the resulting D_e was 301 ± 14 Gy. The counts were significantly lower for decay of the poly mineral fine grains resulting in larger errors on the dose response curve, however both techniques produced coeval results within errors.

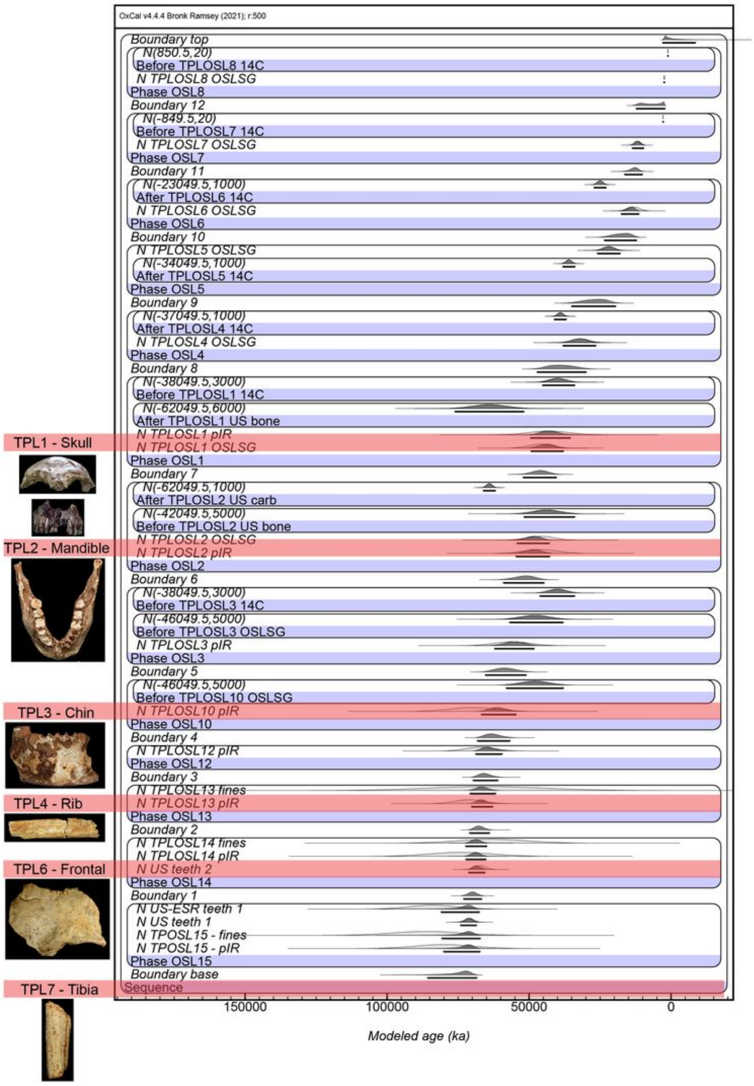

Figure 5

Modeling of the new TPL chronology- All 33 radiometric age estimates from TPL (n = 33) have been incorporated into this Bayesian model, which is presented at 2 sigma error margin. The sample names and layers have been entered into the left and correspond with those found on the stratigraphic drawing (Fig 3). The boundaries represent the borders between each layer and the phases represents each layer, the location of each hominin find; TPL1-7 have also been marked for reference.

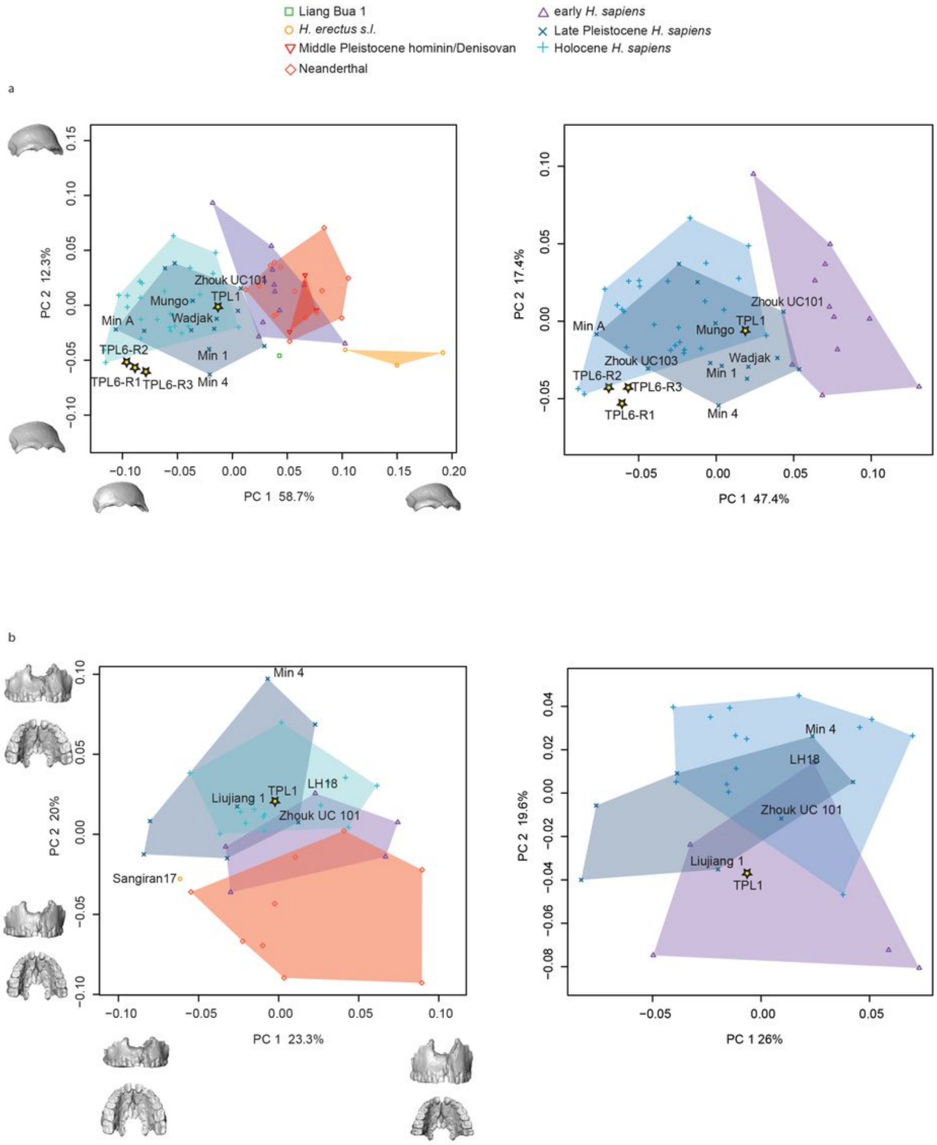

Figure 6

Principal component analyses of Tam Pà Ling hominins frontal and maxillary shape. Shape changes were visualized along PC 1 and PC 2 by warping the sample mean shape along the positive and negative ends of PC 1 and PC 2, plus/minus two standard deviations from the sample mean; Zhoukoudian Upper Cave 101 (Zhouk UC101), Minatogawa (Min) 1, 4, A; Laetoli Hominin 18 (LH18). **A -** TPL 1 and 6 (3 reconstructions TPL6-R1, R2, R3) frontal shape; left panel complete sample and right panel only *H. sapiens*. Shape changes along PC 1 are the projection and shape of the brow ridge, and rounding of the frontal squama, with specimens plotting at the positive end of PC 1 (i.e., *H. erectus*) expressing an entirely more robust and projecting brow ridge, narrower frontal width, and a flatter and more receding frontal squama. Specimens plotting along the negative end of PC 1, including TPL 6, have a morphology that is more gracile and a vertical frontal bone. Shape changes along PC 2 are in the shape of the frontal squama, frontal width, and middle and lateral brow ridge projection. **B -** TPL 1 maxilla shape; left panel complete sample and right panel only *H. sapiens*. Shape changes along PC 1 are mainly in the supero-inferior height of the lower maxilla and the length of the dental arcade. The taller maxillae with shorter dental arcades plot along the positive end. Shape changes along PC2 are in the projection of the lower anterior maxilla and breadth of the palate.

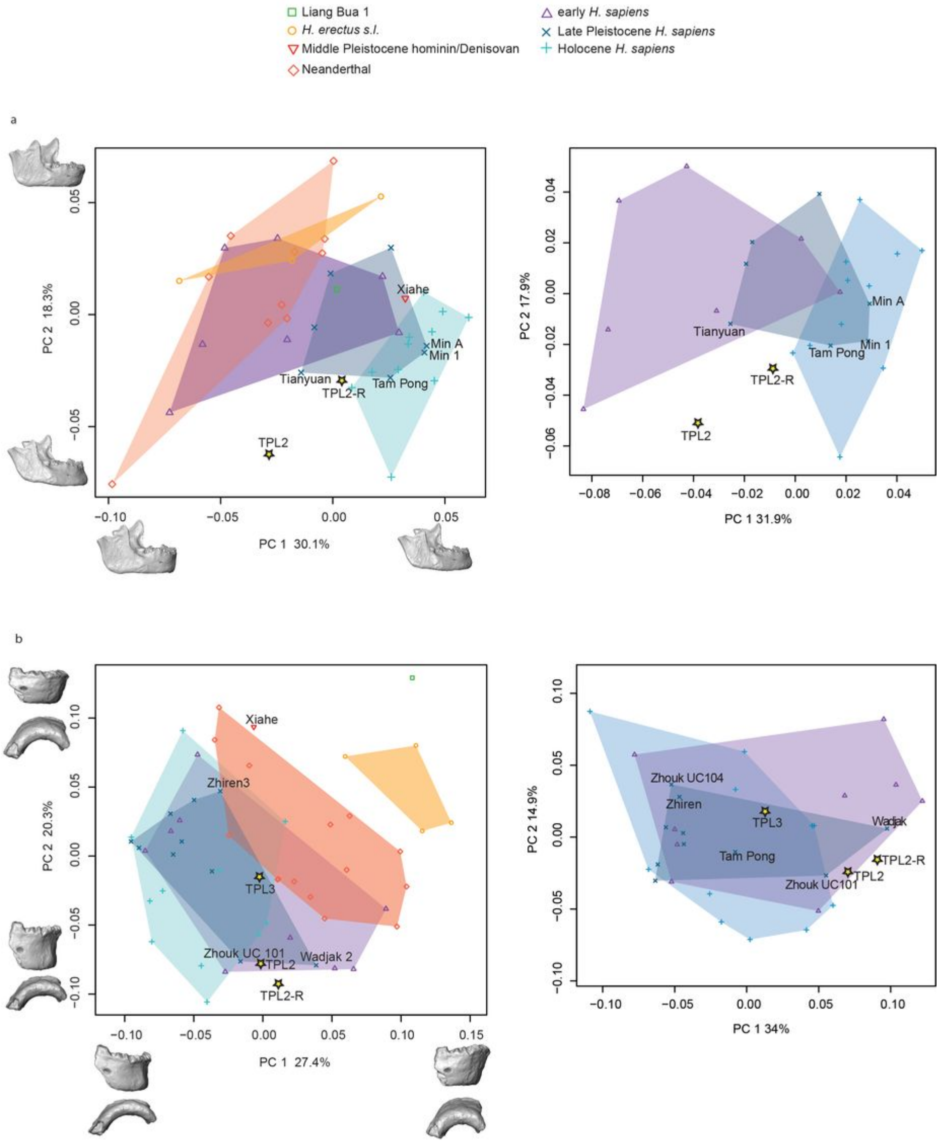

Figure 7

Principal component analyses of Tam Pà Ling hominins mandibular. Shape changes were visualized along PC 1 and PC 2 by warping the sample mean shape along the positive and negative ends of PC 1 and PC 2, plus/minus two standard deviations from the sample mean; Zhoukoudian Upper Cave 101 (Zhouk UC101). **A -** TPL 2 mandible shape (2 reconstructions TPL2, TPL2-R); left panel complete sample and right panel only *H. sapiens.* Shape changes along PC 1 include the width of the mandible, height of anterior symphysis, thickness of the lateral corpus, height and width of ramus, height and size of the coronoid process, and position of mental foramen. Shape changes along PC 2 emphasize the presence of a chin, corpus thickness, and angle and orientation of the ramus. Specimens plotting at the negative end of PC 2 (primarily Neanderthals, *H. erectus*, several early *H. sapiens*) have a vertical anterior symphysis that lacks a chin, thin corpus, and wide and vertically oriented posterior ramus. Whereas specimens plotting at the positive end of PC 2, Qafzeh 9 and a Holocene *H. sapiens*, as well as the original reconstruction of TPL 2, show the opposite pattern. **B -** TPL 2 (2 reconstructions TPL2, TPL2-R) and 3 anterior corpus shape; left panel complete sample and right panel only *H. sapiens.* Shape changes along PC 1 relate to the expression of the chin, and angle and height of the symphysis. Specimens plotting along the negative end of PC 1 (early, Late and Holocene *H. sapiens*) have a pronounced chin and a shorter symphysis height; whereas *H. erectus* and Liang Bua have a taller, receding symphysis that lacks a chin. Both TPL 2 reconstructions and TPL 3 are similar in this morphology expressing a condition intermediate between the extremes. PC 2 also relates to the expression of the chin, and height and robusticity of the anterior corpus. Specimens plotting along the positive end of PC 2 (including both TPL 2 reconstruction) have a taller and thinner corpus with a chin, while TPL 3 has a less pronounced chin and shorter corpus height.

Supplementary Files

This is a list of supplementary files associated with this preprint. Click to download.

- rs.pdf
- FreidlineTPLSupplementary.docx